Working Title:

Combined measurements of proteome and cell turnover reveal the influences of tissue context and pathological aging on protein and organelle lifetimes

Authors: John Hasper[1], Kevin Welle[2], Jennifer Hryhorenko[2], Sina Ghaemmaghami[2,3], Abigail Buchwalter[1,4,5]

Affiliations:

[1]Cardiovascular Research Institute, University of California, San Francisco, San Francisco, CA
[2]University of Rochester Mass Spectrometry Resource Laboratory, Rochester, NY
[3]Department of Biology, University of Rochester, Rochester, NY
[4]Department of Physiology, University of California, San Francisco, San Francisco, CA
[5]Chan Zuckerberg Biohub, San Francisco, CA

Abstract

The lifespans of proteins can range from moments to years within mammalian tissues. Protein lifespan is relevant to organismal aging, as long-lived proteins can accrue damage over time. It is unclear how protein lifetime is shaped by tissue context, where both cell division and proteolytic degradation contribute to protein turnover. Here, we develop turnover and replication analysis by ^{15}N isotope labeling (TRAIL) for parallel quantification of protein and cell lifetimes. We deploy TRAIL over 32 days in 4 mouse tissues to quantify cell proliferation with high precision and no toxicity and determine that protein lifespan varies independently of cell lifespan. Variation in protein lifetime is non-random: multiprotein complexes such as the ribosome have consistent lifetimes across tissues, while mitochondria, peroxisomes, and lipid droplets have variable lifetimes across tissues. To model the effects of aging on tissue homeostasis, we apply TRAIL to progeroid mice and uncover fat-specific alterations in cell lifetime and proteome composition, as well as a broad decrease in protein turnover flux. These data indicate that environmental factors influence protein turnover *in vivo* and provide a framework to understand proteome aging in tissue context.

Introduction

The cellular proteome undergoes constant cycles of synthesis, folding, and degradation. Proteostasis (protein homeostasis) is achieved by the balance of these processes. When these systems function properly, the health of the proteome is ensured by the efficient degradation of misfolded or damaged proteins and replacement with properly folded and functional copies. When proteostasis breaks down due to aging or disease, proteome disruptions including accumulation of oxidative damage, misfolding, and aggregation result[1,2]. Measurements of protein turnover have revealed that protein lifetimes range from minutes to years within mammalian tissues[3–7]. The functional consequences of age-linked proteostasis collapse are most evident for extremely long-lived proteins in post-mitotic tissues. For instance, crystallin proteins of the eye lens misfold and aggregate over decades, causing cataracts[8], while the extremely long-lived nuclear pore complex becomes leaky and dysfunctional in the aging brain[9]. These striking examples raise several questions, including: what factors control protein lifetime in healthy tissues? What is the relationship between protein longevity and cellular longevity? Why do age-linked declines in long-lived protein function manifest only in some tissues?

Protein lifetime is influenced by sequence-encoded features[10]. For instance, proteins with long disordered segments are generally more short-lived than proteins that adopt a stable structure[11,12]. Post-translational modifications have varied effects on protein stability[13,14], while higher buried surface area correlates with longer lifetime[15]. There are many exceptions that break these rules, however, and it is unclear to what extent structural features alone can predict protein lifetime.

Protein lifetime also appears to be influenced by tissue context. Protein turnover rates vary widely across mammalian tissues, and the rate of cell division is thought to accelerate protein turnover by dilution[3,5] (Fig. 1A). However, recent work hints that cell cycle-independent factors also modulate protein lifetime. For instance, the proteome of neurons is more long-lived than the proteome of glia, in spite of the fact that both of these cell types are post-mitotic[5,16]. Protein lifespan also appears to be linked to organismal lifespan, as proteins turn over more slowly in cultured cells isolated from longer-lived animals[17,18]. Altogether, these observations suggest that interactions between proteins and the cellular environment influence protein lifetime.

To define the relationship between protein longevity and cellular longevity, a method that can quantify both of these parameters in parallel is needed. This would make it possible to quantify the contribution of cell proliferation to protein turnover *in vivo*, and could be used to explore how environment, aging, and disease affect tissue homeostasis. While labeling with non-toxic ^{13}C or ^{15}N isotopes has become

69 the gold standard for the quantification of protein turnover rates[3,19], this methodology has not been
70 integrated with cell turnover measurements. Instead, cell turnover rates are frequently measured by partial
71 labeling with nucleotide analogs (e.g. ^{3}H-thymidine or BrdU) or isotopes (e.g. D_2O[20]), which are limited by
72 label toxicity[21–23]. Here, we describe methods to decipher both protein turnover and cell division within
73 mammalian tissues using a single source of label: the stable isotope ^{15}N (Fig. 1B). We name this suite of
74 methods "turnover and replication analysis by isotope labeling", or TRAIL. We apply TRAIL to proliferative
75 and non-proliferative tissues and generate a rich dataset that reveals tissue-specific features of
76 proteostasis. We report that protein and organelle lifetimes vary widely across healthy tissues even after
77 correcting for cell proliferation rates. While the molecular control of these differences in protein and
78 organelle stability across tissues is unknown, this observation implies that aging affects proteostasis in
79 protein- and tissue-specific ways. To model the effects of aging on tissue homeostasis, we applied TRAIL
80 to a mouse model of the pathological accelerated aging disease Hutchinson-Gilford progeria syndrome

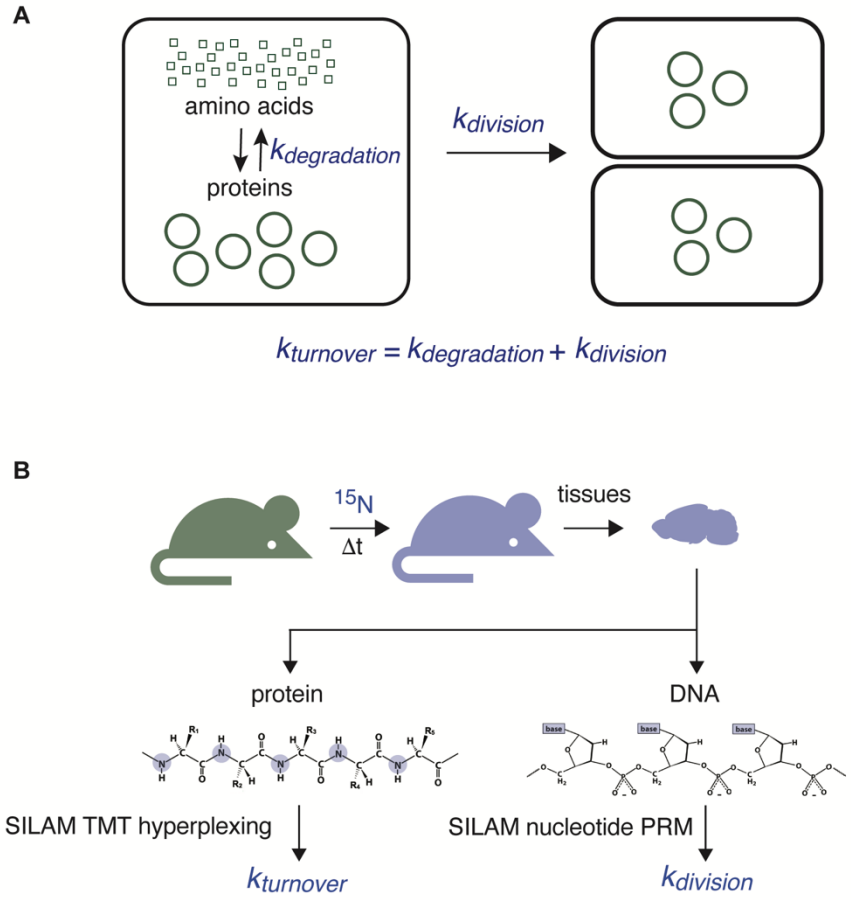

Figure 1. (A) The rate of protein turnover (k_t) is affected both by proteolytic degradation processes within cells (degradation rate, k_{deg}) and by dilution during cell division (cell division rate, k_{div}). (B) Diagram of turnover and replication analysis by isotope labeling (TRAIL) approach for quantifying protein clearance rate (k_t) by tracking protein isotope incorporation and cell division rate (k_{div}) by tracking genomic DNA isotope incorporation. These two measurements are then used to determine the cell-cycle-corrected degradation rates (k_{deg}) for tissue proteomes.

81

82 (HGPS)[24] and uncover both tissue-specific changes to cell lifetime and a proteome-wide decline in protein
83 turnover flux. This work demonstrates how paired protein and cell turnover measurements can reveal basic
84 gaps in our understanding of proteostasis and reveal consequences of pathological aging on the proteome.
85

86 **Results**

87

88 **Increasing throughput of stable isotope labeling timecourses by tandem mass tag multiplexing**

89 Proteome-wide quantification of protein stability can be achieved *in vivo* by feeding mice a food
90 source containing ~100% abundance of the stable, non-toxic isotope ^{15}N, a method referred to as stable
91 isotope labeling in mammals (SILAM)[3,19]. Labeled tissues are then analyzed by tandem mass spectrometry
92 (LC-MS/MS) to quantify the incorporation of labeled amino acids into the proteome over time[3,19]. Broader
93 application of SILAM has been limited by the investment of resources and time required to complete these
94 types of analyses. One major bottleneck is mass spectrometer run time, which rapidly multiplies when
95 each sample must be analyzed in a separate LC-MS/MS run. Further, protein "dropout" due to missing
96 values limits the number of proteins whose turnover kinetics can be precisely determined. We have
97 previously used tandem mass tagging (TMT) to "hyperplex" pools of isotope-labeled samples in a single
98 LC-MS/MS run, which decreases cost while increasing speed and sensitivity[25]. Here, we adapt this
99 approach to ^{15}N-labeled samples from mouse tissue (TMT-SILAM, Fig. 2A). Hyperplexed analysis of ^{15}N-
100 labeled samples presents a unique challenge due to the high complexity of the labeled peptide spectra.
101 The gradual labeling of the *in vivo* amino acid precursor pool by ^{15}N results in broadened MS1 spectra
102 whose average mass to charge ratios increase as a function of labeling time[3], creating a challenging
103 analysis problem that requires specialized data analysis workflows[26,27]**.** However, we previously
104 demonstrated that hyperplexed sample analysis can be simplified by quantifying the relative decay of
105 unlabeled peaks as a function of time rather than the fractional population of unlabeled and labeled
106 peaks[25]. Here, by quantifying the rate of loss of ^{14}N peptides over time of ^{15}N pulse-labeling, we were able
107 to directly measure the turnover rate (k_t) of pre-existing unlabeled proteins (Fig. 2A).
108

109 We performed a 32-day TMT-SILAM time course on young adult (9-week-old) mice and analyzed
110 the labeling kinetics of thousands of proteins per tissue (Supplementary Fig. 1). We focused our analyses
111 on selected tissues that are thought to be either proliferative or post-mitotic[28]: the large intestine (a
112 proliferative tissue); the liver (a quiescent tissue that can proliferate in response to injury); and the heart
113 and white adipose tissue, which are mostly post-mitotic. We filtered these data at several levels to ensure
114 high quality. Experimental replicates were first filtered based on coverage: only proteins that were detected
115 with a minimum of 3 peptide spectral matches (PSMs) in all channels were retained for further analysis.
116 Second, aggregated replicate data were used to determine k_t by least squares fitting to a first order kinetic

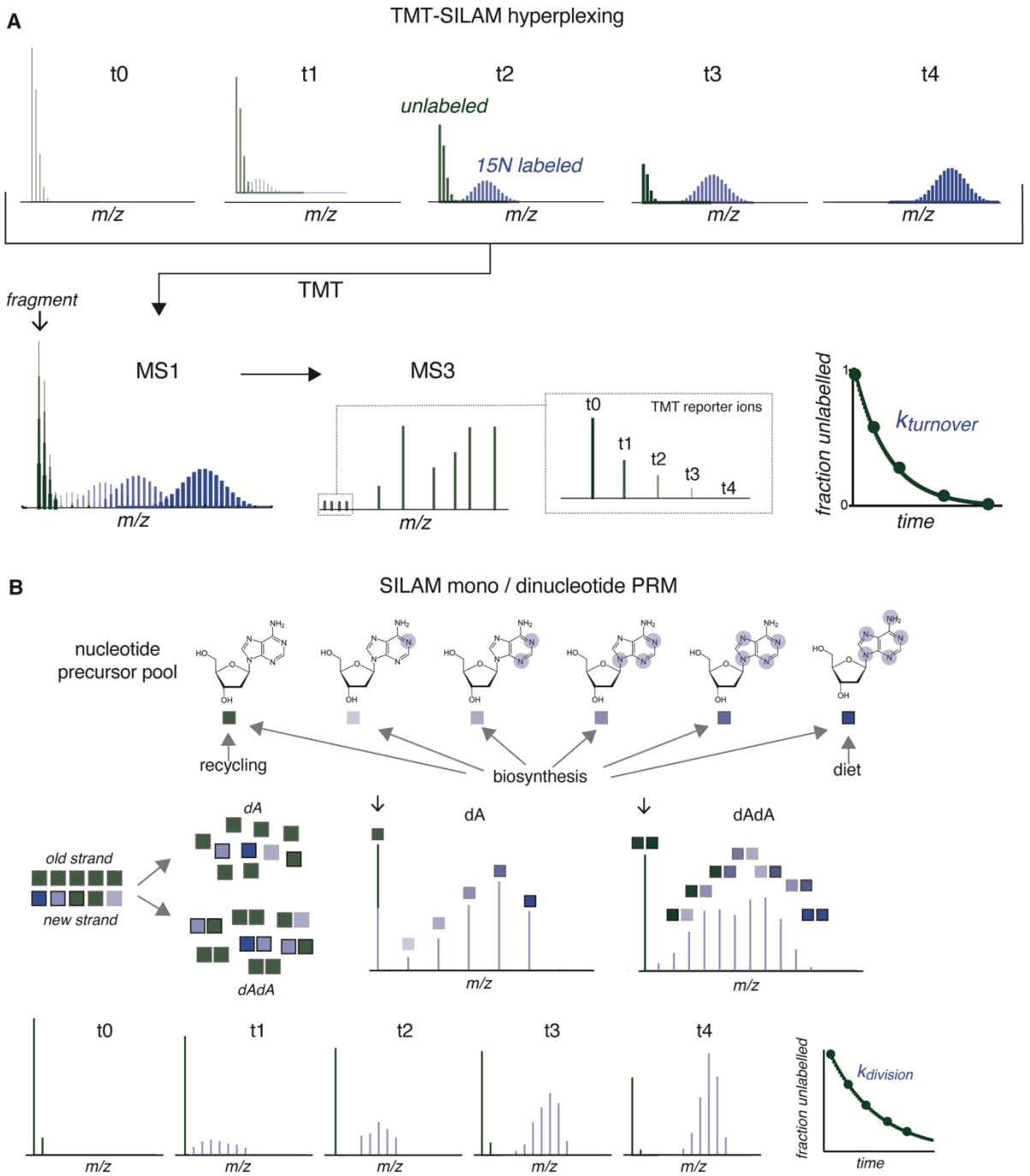

Figure 2. (A) Schematic of TMT-SILAM hyperplexed determination of k_t by tracking the rate of loss of unlabeled peptides over time. Samples from multiple timepoints are hyperplexed by conjugation with unique TMT tags and combined into a single sample before LC-MS/MS. A peptide detected in multiple time points will have a single m/z in MS1, but will fragment into reporter ions with distinct masses in MS2/MS3. Quantification of SILAM-unlabeled MS3 peaks reveals the kinetics of loss of the unlabeled peptides, which can be fit to determine k_t. (B) Schematic of SILAM mono and dinucleotide PRM. The relative isotope abundance (RIA) of the nucleotide precursor pool reflects the rates of precursor uptake, biosynthesis, and recycling of pre-existing nucleotides. By quantifying the abundances of unlabeled, partially labeled, and fully labeled dinucleotides in genomic DNA, the extent of unlabeled nucleotide recycling can be inferred and can be used to determine corrected cell division rates (k_{div}).

model. Only k_t values that were fit to data arising from at least 2 replicates with a high goodness of fit (t-statistic > 3) were considered in downstream analyses.

120 **Features of protein turnover across tissues**

121 Altogether, we defined high-confidence k_t values (Fig. 3A) and corresponding predicted half-life
122 ($t_{1/2}$) values (Fig. 3B) for thousands of proteins per tissue: 2719 in the large intestine, 2099 in liver, 1610 in
123 white adipose tissue, and 1635 in the heart (Supplementary Fig. 1). The distributions of k_t values were
124 unique for each tissue; proteins were more short-lived in the intestine (median $t_{1/2}$ 1.7 days) and liver
125 (median $t_{1/2}$ 2.4 days), but more long-lived in the fat (median $t_{1/2}$ 6.1 days) and heart (median $t_{1/2}$ 5.7 days).
126 Protein abundance and protein lifetime were not correlated with each other (Supplementary Fig. 2).
127 Specific protein features have been previously reported to correlate with more rapid protein turnover. For
128 instance, a greater extent of protein disorder correlates with shorter protein lifetime in yeast and in
129 mammalian cell culture[11,12]. We evaluated the turnover rates of an experimentally validated list of
130 disordered proteins from the DisProt database[29] and saw that in some cases, disordered proteins turned
131 over significantly faster than the proteome median (Supplementary Fig. 3A). However, disordered proteins
132 as a class do not turn over significantly faster than the proteome median (Supplementary Fig. 3B). Instead,
133 disordered proteins may be rapidly degraded in one tissue but relatively stable in another, suggesting that
134 the interplay of sequence features and environmental factors influences protein lifetime.
135
136 We explored and excluded several potential explanations for tissue-specific differences in protein
137 stability. (1) These differences persist among the subset of proteins whose lifetimes were quantified across
138 all four tissues (902 proteins total; Supplementary Fig. 3C,D), indicating that differences in protein lifetime
139 are not due simply to differences in proteome composition. (2) These differences also persist if secreted
140 proteins are excluded from analyses (Supplementary Fig. 3E-G); secreted proteins are a unique class of
141 proteins whose turnover is difficult to accurately profile by pulse-chase experiments, as their sites of
142 synthesis, function, and degradation can be quite disparate. Even after controlling for these factors,
143 differences in protein lifetimes across tissues are readily apparent. For example, many intracellular proteins
144 have days-long lifetimes in the liver but weeks-long lifetimes in the heart (Fig. 3C).
145
146 We looked more closely at intracellular proteins at the extremes of stability by identifying gene
147 ontology (GO) terms that were over-represented in either the top decile (Fig. 3D) or bottom decile (Fig. 3E)
148 of k_t values in each tissue. The identity of the most short-lived and most long-lived proteins varies widely.
149 For instance, proteins involved in intestinal nutrient absorption are enriched among the most short-lived
150 proteins of the large intestine, while proteins involved in alcohol and fatty acid metabolism are found among
151 the most short-lived proteins of the liver (Fig. 3D). At the other extreme, components of chromatin are
152 enriched in the most long-lived proteins of the liver and intestine, while proteins involved in various
153 mitochondrial functions are enriched in the most long-lived proteins of the heart and adipose tissue (Fig.

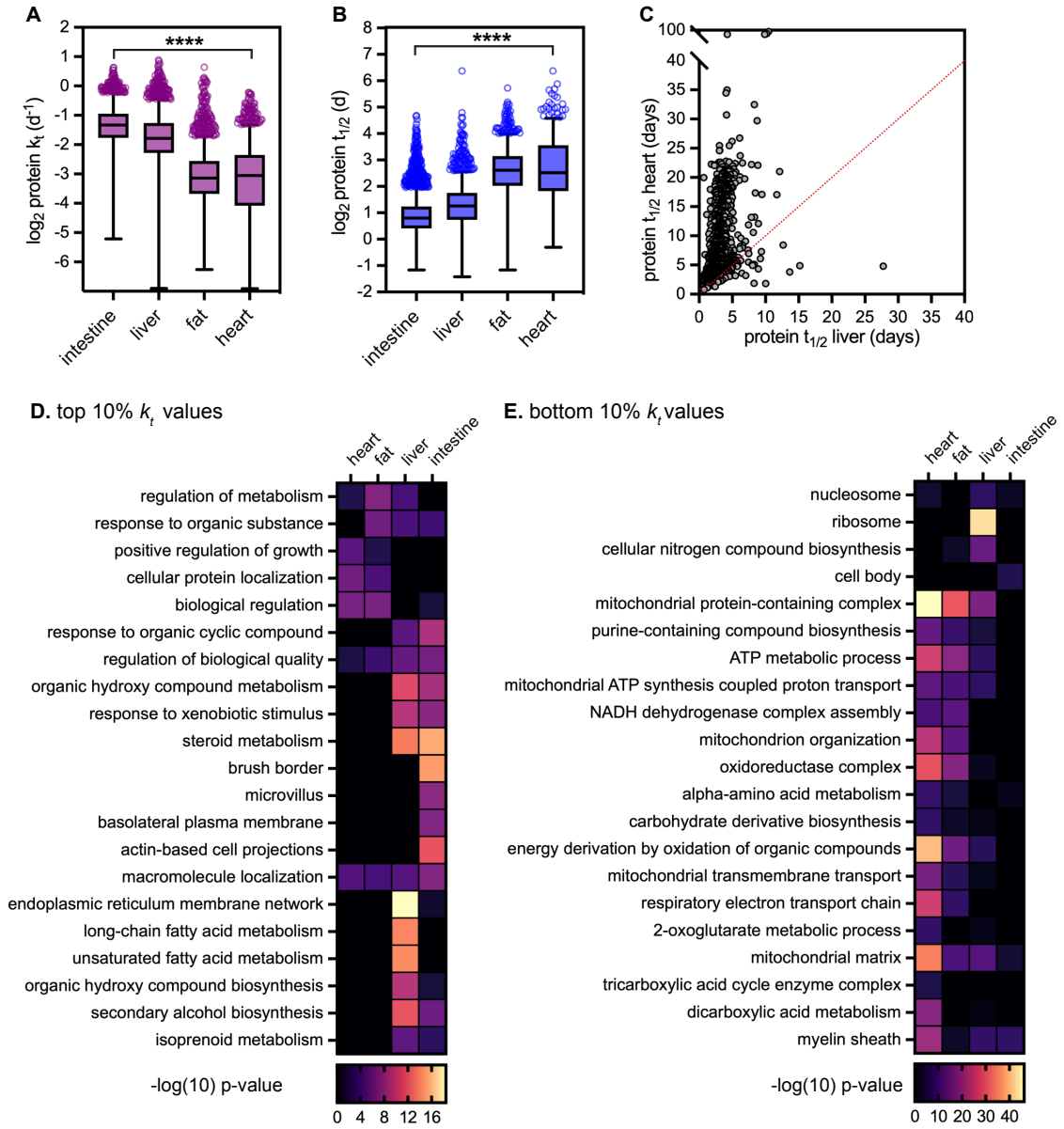

Figure 3. Proteome turnover measurements for four reference tissues. (A) Clearance rates (k_t) and (B) predicted half-lives ($t_{1/2}$) determined by SILAM-TMT of proteins extracted from intestine (n = 2719; median $t_{1/2}$ 1.7 days), liver (n = 2099, median $t_{1/2}$ 2.4 days), fat (n = 1610, median $t_{1/2}$ 6.1 days), and heart (n = 1635, median $t_{1/2}$ 5.7 days). Box (Tukey) plot center line indicates median; box limits indicate 25th to 75th percentiles; whiskers indicate 1.5x interquartile range; points indicate outlier values. **** indicates that all medians are significantly different ($p < 0.0001$, Kruskal-Wallis test). See also Supplementary Table 1 for full dataset. (C) Predicted half-lives ($t_{1/2}$) for 1102 intracellular proteins in the heart versus the liver. (D-E) Heatmaps of GO term enrichment in the top 10% (least stable, D) and the bottom 10% (most stable, E) of k_t values for intracellular proteins detected in each tissue.

3E). Interestingly, while components of chromatin and mitochondria have been found to be long-lived in other protein turnover studies[3,5,30,31], our data suggest that their stability varies from tissue to tissue.

Rates of protein turnover are influenced both by proteolytic degradation of proteins and by dilution of proteins during cell division (Fig. 1A). Differences in protein stability have been previously reported

between mammalian tissues, such as the brain and the liver[3,5]. Variation in the extent of cell proliferation across tissues could underlie this difference, as protein dilution during cell division would accelerate the apparent protein turnover rate. However, proteome lifetimes also differ significantly between non-dividing cell types[5,16], as well as in the same cell type (fibroblasts) isolated from different mammals[17]. These observations suggest that protein lifetime may be influenced by cellular and/or tissue context independently of cell proliferation. However, to define the relationship between protein lifetime and cellular proliferation, a method that can quantify both of these parameters in parallel is needed.

Turnover and replication analysis by isotope labeling (TRAIL) to profile cell and protein turnover

We sought to develop a method to quantify cell proliferation rates in parallel with protein turnover measurements. While ^{15}N-labeled amino acids supplied via SILAM chow have been widely used to label proteins, ^{15}N-labeled nucleic acids are also present in SILAM chow (Supplementary Fig. 4), and diet-supplied ^{15}N robustly incorporates into genomic DNA[32]. We therefore reasoned that tracking the rate of ^{15}N incorporation into the genome via DNA replication would yield cell division rates (k_{div}) (Fig. 1B, Fig. 2). Importantly, ^{15}N labeling is tolerated at a far higher dose and for a far longer time (over multiple generations[19]) than other widely used labels that incorporate into replicating DNA, such as ^{3}H-thymidine[22], BrdU[21], or D_2O[23]. This opens the possibility of precise measurement of cell lifetimes over long timescales. This measurement can also be used to control for the influence of cell proliferation on protein turnover rates by subtracting k_{div} from k_t to determine corrected protein degradation rates (k_{deg}). We refer to this group of methods as turnover and replication analysis by isotope labeling (TRAIL).

To develop this approach, we first needed to address a technical barrier. The fractional labeling of genomic DNA during a pulse-labeling experiment is influenced both by the rate of replication and by the relative isotope abundance (RIA) of the precursor nucleotide pool (Fig. 2B). The latter is strongly influenced by precursor uptake from the diet, nucleotide biosynthesis, and nucleotide recycling *in vivo*[33]. Incomplete labeling of the precursor pool due to low precursor uptake, slow *de novo* biosynthesis, or extensive recycling of pre-existing nucleic acids would decrease the extent of ^{15}N incorporation into newly replicated genomic DNA[32]. Further, the relative contributions of each of these factors may vary across tissues. Altogether, this means that one must define the RIA of the precursor nucleotide pool in each tissue in order to accurately determine the rate of replication by measuring the fractional labeling of genomic DNA.

We reasoned that we could deconvolute the RIA of the precursor nucleotide pool by analyzing the combinatorics of labeling in contiguous stretches of *dinucleotides* obtained from the same strand of

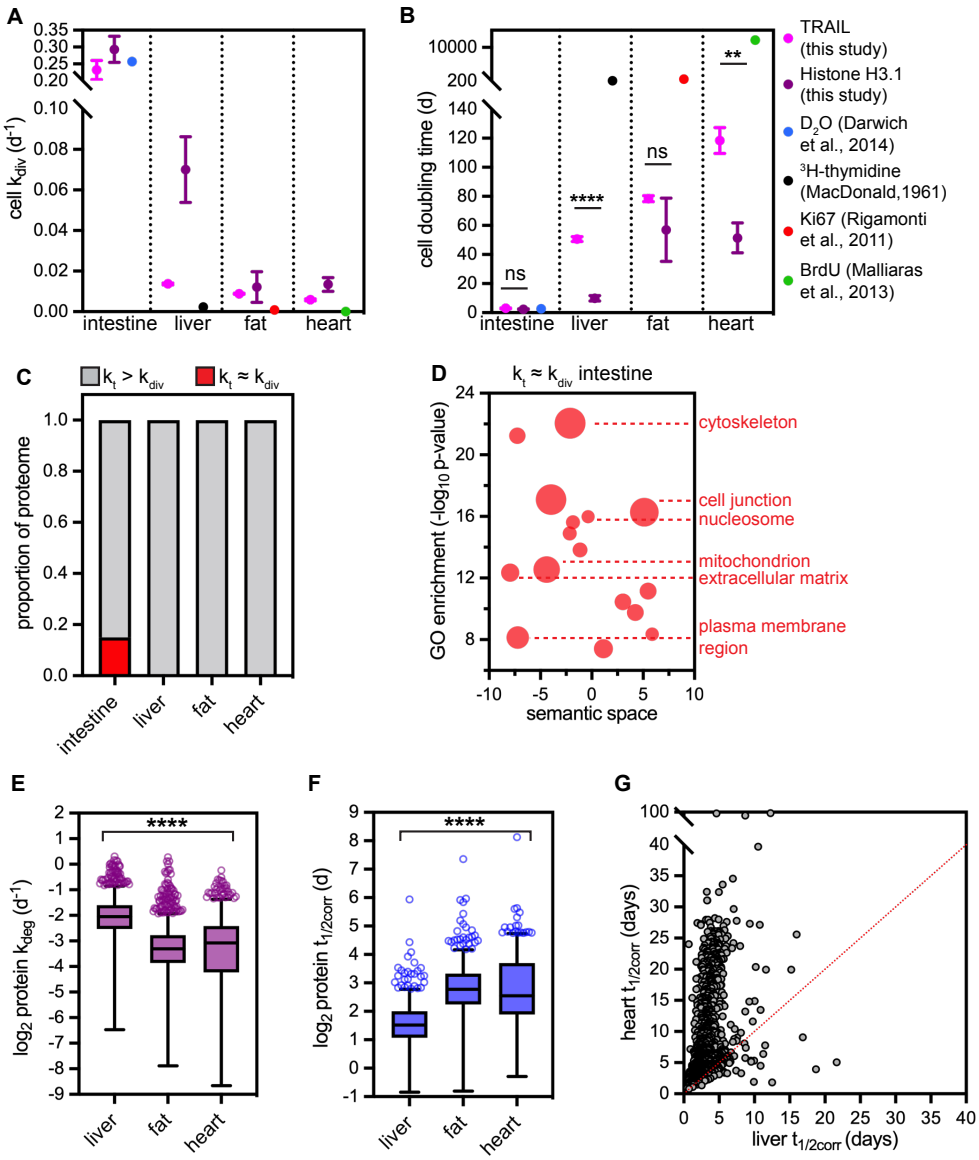

Figure 4. (A-B) Comparison of cell division rate (k_{div}, (A)) and cell doubling time (B) in intestine, liver, fat, and heart, determined by TRAIL (our study); by Histone H3.1 protein turnover (our study); and previously published reports by a range of methods, including ^{3}H-thymidine labeling, BrdU pulse-labeling, D_2O water labeling, and Ki67 staining. Error bars indicate SEM. Data reproduced from meta-analysis by Sender & Milo Nature Medicine 2021. * indicates $p < 0.05$ for k_{div} determined by TRAIL versus H3.1 turnover in the liver (unpaired t-test). See also Supplementary Table 3 for full dataset. (C) Only the proliferative intestine has a significant number of proteins whose k_t is equivalent to k_{div}, suggesting that these proteins are diluted by cell division. (D) A subset of Gene Ontology (GO) terms (cellular component) over-represented in proteins that are diluted out by cell division in the intestine are shown in a bubble plot. Redundant GO terms were removed and non-redundant GO terms were organized based on semantic similarity by REViGO. Bubble size corresponds to number of proteins associated with GO term. (E) Cell-cycle-corrected degradation rates (k_{deg}) and (F) half-lives ($t_{1/2corr}$) for 967 proteins detected in liver (median $t_{1/2}$ 2.9 days), fat (median $t_{1/2}$ 6.8 days), and heart (median $t_{1/2}$ 5.9 days). Box (Tukey) plot center line indicates median; box limits indicate 25th to 75th percentiles; whiskers indicate 1.5x interquartile range; points indicate outlier values. **** indicates that all medians are significantly different ($p < 0.0001$, Kruskal-Wallis test). (G) Predicted cell-cycle-corrected half-lives ($t_{1/2corr}$) for 1102 intracellular proteins in the heart versus the liver. See also Supplementary Table 4 for full dataset.

genomic DNA (Fig. 2B, Supplementary Fig. 5; see Methods). A strand of DNA that has been synthesized in the presence of label will contain labeled nucleotides at a frequency that is contingent on the RIA of the

precursor pool. Analysis of the isotopologue distribution within dinucleotides enables the calculation of the prevalence of recycled unlabeled nucleotides within the precursor pool. Thus, we can determine what fraction of the observed fully unlabeled dinucleotide population was derived from pre-existing unlabeled DNA strands, and what fraction was derived from newly synthesized strands that incorporated unlabeled recycled nucleotides. Through this deconvolution, we can measure the relative ratio of old and newly synthesized DNA and determine the rate of cell proliferation.

We digested genomic DNA from SILAM-labeled mouse tissue to short oligonucleotides using the enzyme benzonase[34], then quantified $^{15}N/^{14}N$ isotope abundance ratios in dinucleotides by mass spectrometry. We found that the ^{15}N RIA of the precursor pool was very high in all tissues, and that diet-derived ^{15}N-labeled nucleic acids were preferentially incorporated into newly synthesized genomic DNA (Supplementary Fig. 5C). This is in line with the fact that nucleotide salvage pathways are repressed in S phase while *de novo* nucleotide synthesis is upregulated, so that cells primarily rely on the latter source of nucleotides for DNA replication[35]. This outcome is also consistent with observations from other modes of DNA pulse labeling[20].

Our finding that diet-derived and de novo synthesized nucleic acids are preferred for DNA replication implies that we can make an accurate measurement of DNA replication rates by tracking ^{15}N incorporation into either mononucleosides or dinucleotides isolated from genome DNA. We tested this by isolating free dA, dC, dT, and dG mononucleosides from genomic DNA by digestion with a cocktail of benzonase, phosphodiesterase, and alkaline phosphatase[36] and quantifying $^{15}N/^{14}N$ isotope ratios by mass spectrometry (see Methods). Decay curves for all four mononucleosides were in close alignment both with each other (Supplementary Fig. 6A) and with dinucleotide curves (Supplementary Fig. 5D), indicating that TRAIL is a highly precise and reproducible method for quantifying DNA replication rate.

With these important controls established, we then applied TRAIL to the large intestine. We determined a doubling time of ~3 days for this proliferative epithelial tissue, in close agreement with previous analyses by orthogonal methods[28,37] (Fig. 4A-B). We then applied this method to the liver, fat, and heart and found that cells of these tissues have very long average doubling times indicating low proliferative capacity (Fig. 4A-B). These data are qualitatively consistent with previous reports of slow proliferation in these tissues[38–40](Fig. 4A-B). Notably, however, analysis of isotope incorporation into both nucleosides and dinucleotides provides far greater precision and accuracy than methods that infer cell doubling time from pulse-labeling with a single nucleotide analog or immunostaining with a cell-cycle-linked antigen.

231 The turnover of Histone H3.1 has been used as a proxy for cell division in protein turnover
232 studies[5,16] because Histone H3.1 is incorporated into nucleosomes as a heterodimer with Histone H4 solely
233 after DNA replication[41], leading to the expectation that this protein's levels would decrease by dilution over
234 successive cell divisions. However, we noted that the lifetime of Histone H3.1 was often shorter than the
235 cell doubling time determined by TRAIL. This distinction was most apparent in the slowly proliferative liver,
236 heart, and fat (Fig. 4A-B). We speculate that this difference reflects DNA replication-independent
237 processes that regulate the lifetime of H3.1. For instance, H3.1/H4 dimers can be evicted from DNA during
238 transcription and are replaced with heterodimers of Histone H3.3 and Histone H4[42]. Separately, histones
239 can also be found in cytosolic pools in complex with chaperones, where they may be more rapidly turned
240 over[43]. We speculate that each of these factors contributes to the turnover of this histone isoform in
241 postmitotic tissues over long timescales. TRAIL thus provides a superior measurement of cell proliferation
242 rates over long timescales and suggests contextual variability in the rate of turnover of the replication-
243 dependent Histone H3.1 across tissues.
244
245 **Protein degradation rates vary across tissues after cell cycle correction**
246 Cellular k_{div} rates can be subtracted from protein k_t values to extrapolate corrected protein
247 degradation rates (k_{deg}) (Fig. 1A). The extreme case where a k_{deg} value approaches zero indicates that
248 dilution by cell division is the major contributor to protein turnover; that is, protein k_t and cellular k_{div} are
249 approximately equal. When we compared these values across tissues, we found that k_{div} was roughly
250 equivalent to k_t for approximately 15% of the intestine proteome (Fig. 4C; Supplementary Fig. 6B). These
251 proteins are components of diverse cellular structures including the cytoskeleton, the extracellular matrix,
252 cell-cell junctions, mitochondria, and chromatin (Fig. 4D). Notably, many of these proteins are also long-
253 lived in postmitotic tissues but turn over at a slow rate that exceeds the rate of cell division. Histone H3.1
254 is one such protein (Fig. 4A-B). This observation implies that long-lived proteins are subject to distinct
255 regimes of protein turnover in proliferative *versus* post-mitotic tissues.
256
257 We next examined k_{deg} values in the slowly proliferative liver, heart, and fat. If variable cell
258 proliferation rates underlie the variability in protein k_t values across these tissues, k_{deg} values should be
259 largely invariant after correcting for k_{div}. We did not observe this outcome. Instead, the range of k_{deg} values
260 remained distinct from tissue to tissue even after correcting for cell proliferation rates, and persisted when
261 we restricted our analysis only to proteins that were detected in all tissues (967 proteins; Fig. 4E-F).
262 Overall, the liver proteome (median $t_{1/2corr}$ 2.9 days) turns over significantly more rapidly than the fat
263 proteome (median $t_{1/2corr}$ 6.8 days) or heart proteome (median $t_{1/2corr}$ 5.8 days) after cell cycle correction
264 (Fig. 4G). These data indicate that protein lifetime is broadly influenced by other environmental factors
265 beyond cell proliferation rate. One potential explanation for these differences could be variation in the

266 composition and activity of protein folding chaperones, the ubiquitin-proteasome system, and/or the
267 autophagy machinery across tissues[44–46].
268
269 **Peroxisomes, lipid droplets, and mitochondria have highly variable lifetimes across tissues**
270 To evaluate the extent of variability in k_{deg} across tissues, we determined the normalized cross-
271 tissue dispersion (*D*) of k_{deg} for the 967 proteins shared across the liver, fat, and heart datasets(see
272 Methods; Supplementary Fig. 7). We then used this metric to dissect variability in protein lifetime across
273 tissues, focusing on constituents of cellular organelles (Fig. 5), multiprotein complexes (Fig. 6) and
274 pathways (Supplementary Fig. 8).

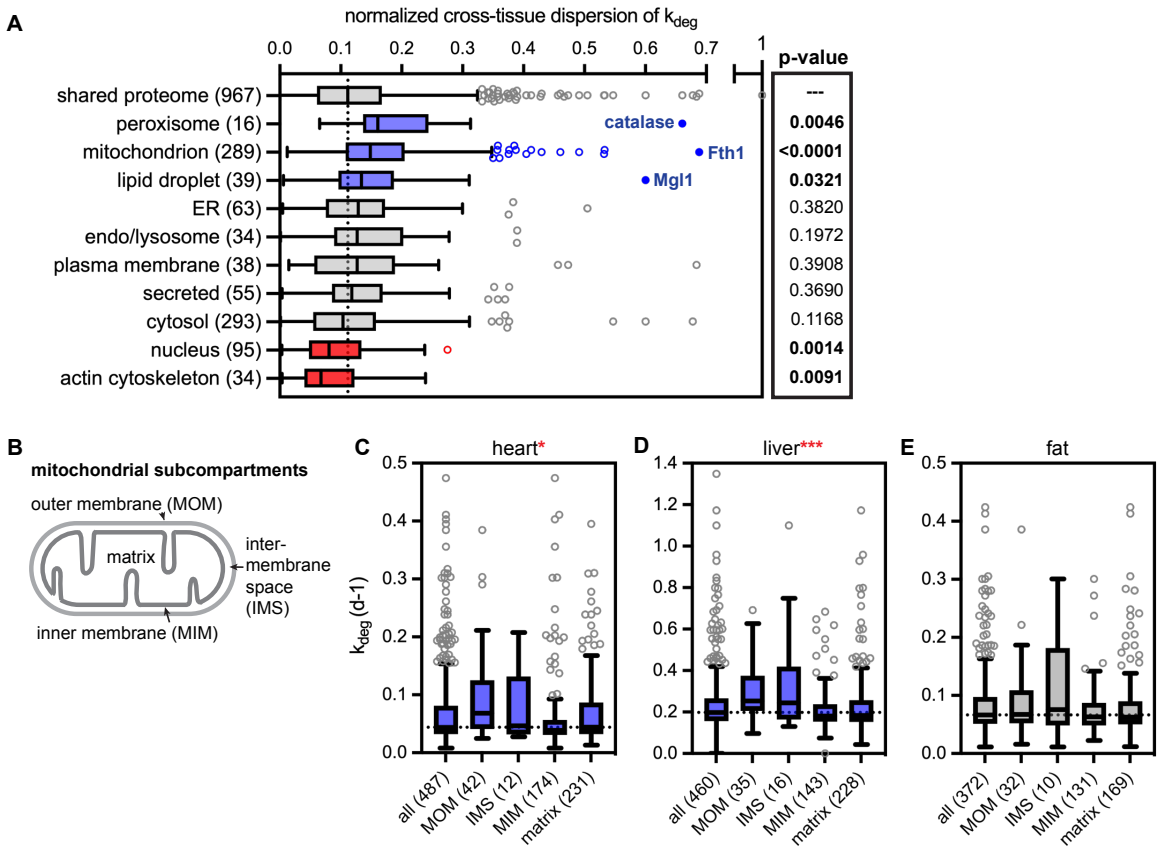

Figure 5. (A) Cross-tissue dispersion analysis of k_{deg} values across heart, liver, and fat by cellular organelle. Blue indicates a subset has a significantly elevated median dispersion of k_{deg} values across tissues; red indicates a subset has a significantly decreased dispersion of k_{deg} values across tissues. Significance determined by Mann-Whitney test. The peroxisomal enzyme catalase, the mitochondrial resident protein Fth1, and the lipid droplet enzyme MGL1 are highlighted as residents of each organelle with the most extremely variable lifetimes across tissues. (B-D) Analysis of k_{deg} rates across mitochondrial sub-compartments. MOM: mitochondrial outer membrane; IMS: intermembrane space; MIM: mitochondrial inner membrane. Numbers indicate total proteins detected in each subcompartment. Proteins of the MOM and IMS turn over significantly faster than proteins of the MIM and matrix in the heart (C) and liver (D). In contrast, all mitochondrial subcompartments turn over at similar rates in the white adipose tissue (E). Significance determined by Kruskal-Wallis test.See also Supplementary Table 5 for full dataset. All box (Tukey) plots: center line indicates median; box limits indicate 25th to 75th percentiles; whiskers indicate 1.5x interquartile range; points indicate outlier values.
275

276 Among proteins that are residents of specific subcellular organelles, components of the actin
277 cytoskeleton and residents of the nucleus have much less variable lifetimes than the proteome as a whole
278 (Fig. 5A-B). In contrast, constituents of peroxisomes, lipid droplets, and mitochondria have significantly
279 more variable lifetimes across tissues than the proteome as a whole (Fig. 5A; Supplementary Fig. 9),
280 implying that the degradative flux of these organelles varies from tissue to tissue. These organelles can
281 be degraded by specialized variants of autophagy termed pexophagy[47], lipophagy[48], and mitophagy[49],
282 respectively.
283
284 Peroxisomes play major roles in lipid catabolism, and their biogenesis is induced by signaling
285 through peroxisome proliferator agonist receptors (PPARs) and other mechanisms. Upon removal of
286 biogenesis-promoting signals, excess peroxisomes are degraded by pexophagy[50]. This process was first
287 documented in the liver; consistently, we observe rapid turnover of peroxisomal proteins in this tissue. Our
288 data indicate that peroxisomes are also degraded rapidly in the intestine but are degraded more slowly in
289 the heart and adipose tissue (Supplementary Fig. 9).
290
291 Lipid droplets (LDs) are the major intracellular sites of lipid storage. In response to nutrient
292 deprivation, LDs mobilize lipids either by lipolysis to generate fatty acids or by lipophagy, which involves
293 delivery of both the protein and lipid components of LDs to the lysosome[51]. Lipophagic flux is high in the
294 liver[48], and we observe rapid degradation of LD proteins in this organ (Supplementary Fig. 9). In contrast,
295 LD proteins are longer-lived in the white adipose tissue and in the heart. This is somewhat unexpected, as
296 adipose tissue rapidly mobilizes free fatty acids when nutrients are low[52], while heart tissue depends on
297 fat oxidation for energy[53]. This outcome indicates that lipophagic flux is lower in these tissues and suggests
298 that fatty acids are instead mobilized from LDs by lipolysis while sparing LD resident proteins from turnover.
299
300 Mitochondria are long-lived organelles in many tissues, including the brain[3,6], heart[54], and skeletal
301 muscle[30,31]. Consistent with these recent studies, we find that mitochondria are long-lived in the heart
302 (median mitochondrial protein $t_{1/2}$ of 18.1 days vs. 5.8 days for total proteome). Mitochondria are also long-
303 lived in the white adipose tissue (median mitochondrial protein $t_{1/2}$ of 10.5 days vs. 6.8 days for total
304 proteome) (Fig. 5C,E). Surprisingly, however, mitochondria turn over more rapidly in the liver (median
305 mitochondrial protein $t_{1/2}$ of 3.5 days vs. 2.9 days for total proteome) (Fig. 5D). This finding suggests major
306 differences in mitochondrial regulation and function in this organ but is consistent with a previous report of
307 high mitophagy flux in the liver using an *in vivo* reporter system[55].
308
309 We achieved high coverage of the mitochondrial proteome, making it possible to inspect the
310 turnover of mitochondrial subcompartments across tissues (Fig. 5B-E). Proteins of the mitochondrial outer

311 membrane (MOM) and the intermembrane space (IMS) generally turn over more rapidly than proteins of
312 internal compartments such as the mitochondrial inner membrane (MIM) and the matrix. This disparity is
313 most apparent in the heart and liver (Fig. 5C,D). A previous analysis of protein lifetimes in the brain similarly
314 reported more rapid turnover of MOM proteins[6]. Notably, the MOM and IMS are accessible to the cytosol
315 while the MIM and matrix are sequestered. These data suggest that selective degradation of MOM/IMS
316 proteins occurs at a significant rate in many tissues, including the heart, liver, and brain[6]. This could be
317 achieved by extraction and delivery to the proteasome, piecemeal autophagy, and/or sequestration into
318 mitochondrial-derived vesicles[56]. In contrast, all mitochondrial subcompartments exhibit coherent turnover
319 in white adipose tissue (Fig. 5E). This could indicate that mitochondria are degraded more frequently by
320 organellar autophagy (mitophagy) than by selective degradation of mitochondrial components in this
321 tissue. Interestingly, mitophagy plays major roles in the differentiation and maintenance of white
322 adipocytes, which characteristically have lower numbers of mitochondria[57]. Altogether, our data indicate
323 that both the overall flux of mitochondrial turnover and the mechanism(s) used to achieve turnover vary
324 across tissues.
325
326 **Multiprotein complex subunits have coherent lifetimes within and across tissues**
327 It has been suggested that participation in stable multiprotein complexes might protect proteins
328 from degradation and extend protein half-life[15,58]. We evaluated the degradation kinetics of 12 multiprotein
329 complexes for which at least 5 subunits were detected in all four tissues and found that in general,
330 multiprotein complex subunits do not exhibit significantly lower degradation rates than the proteome
331 median (Fig. 6A-B). This indicates that participation in a stable multiprotein complex is not sufficient to
332 dramatically extend protein lifetime. It is important to note, however, that this steady-state measurement
333 cannot determine whether complex subunits are selectively degraded if they fail to assemble correctly after
334 synthesis[58].
335
336 Some multiprotein complexes have been reported to exhibit coherent subunit turnover, perhaps
337 reflecting their stable association from biogenesis to degradation[7]. To determine whether complex subunits
338 exhibit more similar turnover rates than would be expected by random chance, we calculated the intra-
339 tissue k_{deg} dispersion *(d)* for multiprotein complexes for which at least 5 subunits were detected (12-24
340 complexes per tissue). For comparison, we calculated *d* for an equivalent number of randomly chosen
341 proteins (Fig. 6C,D). Comparing these values indicated that most multiprotein complexes turn over
342 coherently in the liver, heart, and fat, while this difference was not significant in the intestine. Consistent
343 with a previous report[7], we also find that the CCT/TriC chaperonin complex is an outlier whose subunits
344 have extremely consistent k_{deg} values (low *d,* Fig. 6C, solid blue). Other multiprotein complexes with
345 coherent turnover include the ribosome, proteasome, oligosaccharyltransferase (OST) complex, and the

346 mitochondrial respiratory chain complexes (Fig. 6D). In striking contrast, the spliceosome is an outlier

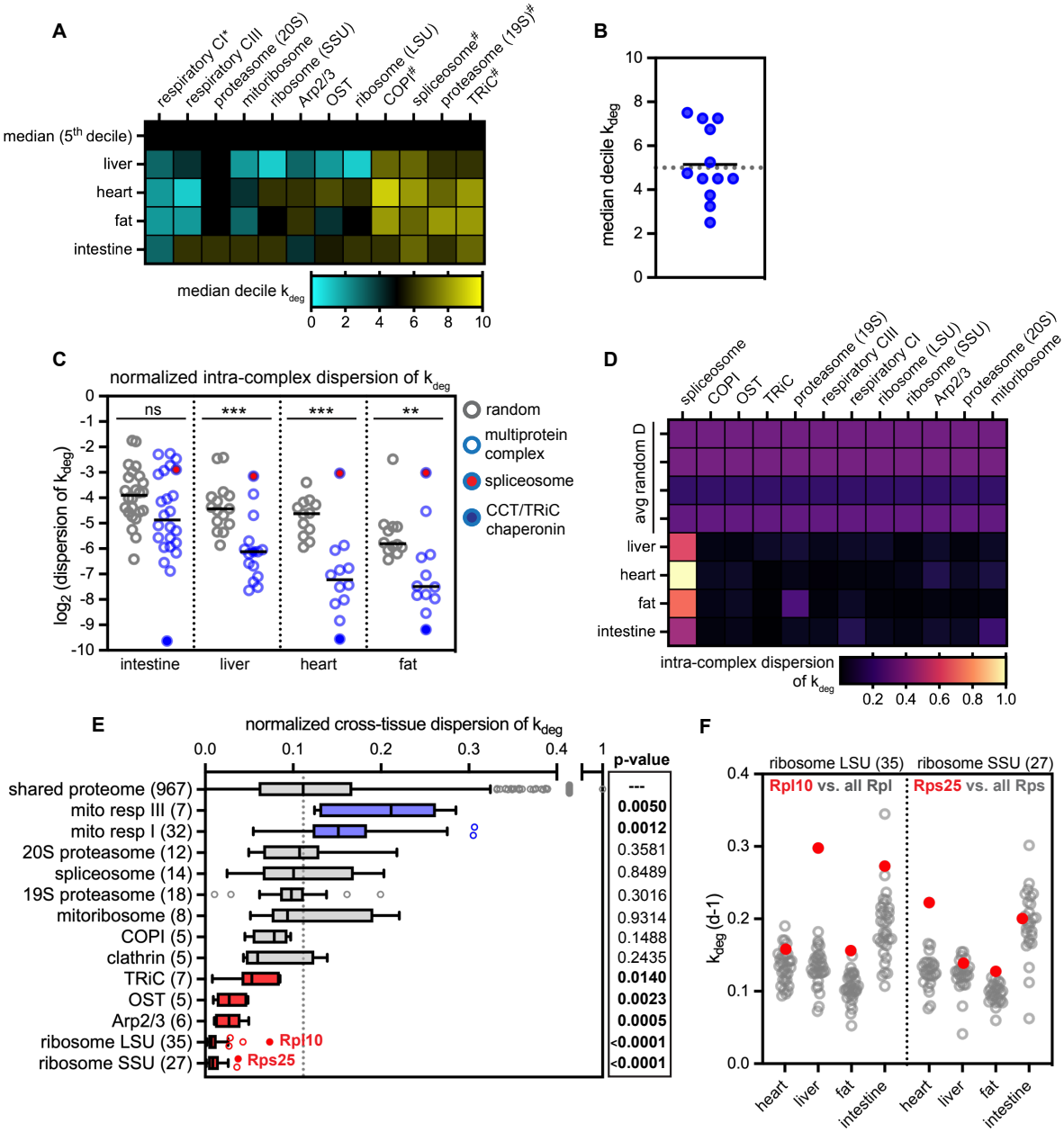

Figure 6. (A) The median decile of k_{deg} for each multiprotein complex with at least 5 subunits detected. *indicates complexes that turn over significantly more slowly, and #indicates complexes that turn over significantly faster than the proteome median in all tissues. (B) Median decile k_{deg} for multiprotein complexes (black bar) does not deviate from the proteome median (5th decile). (C) Intra-complex dispersion was computed for complexes with at least 5 subunits detected (blue) and a random dispersion value was calculated by computing dispersion for an equivalent number of randomly chosen proteins (gray).Black bar, median. In liver, heart, and fat, complexes exhibit a significantly lower intra-complex dispersion than would be expected by chance (** $p<0.01$; *** $p < 0.001$, Mann-Whitney test). The spliceosome (red) is an outlier with high intra-complex dispersion; the TriC/chaperonin complex (solid blue) is an outlier with low intra-complex dispersion. (D) heatmap of intra-complex dispersion across tissues. (E) Analysis of normalized cross-tissue dispersion of k_{deg} by multiprotein complex. P-values indicate significance of deviation from proteome mean (Mann-Whitney test). While the small and large subunits of the ribosome have extremely low cross-tissue dispersion, outlier subunits Rps25 and Rpl10 have more variability across tissues (solid red). Box (Tukey) plot center line indicates median; boxes indicate 25th to 75th percentiles; whiskers indicate 1.5x interquartile range; points indicate outlier values. (F) k_{deg} values of ribosome subunits. See also Supplementary Table 5 for full dataset.

347

348 whose components have widely varying k_{deg} values (high *d*; Fig. 6C, solid red; Fig. 6D). We speculate that
349 this may reflect the cyclical, activity-coupled nature of spliceosomal assembly[59], and may indicate that
350 individual spliceosome subcomplexes undergo quality control / degradation at various rates.
351
352 We next asked whether multiprotein complex lifetimes are consistent or variable across tissues by
353 calculating the cross-tissue k_{deg} dispersion *(D)* of individual subunits across the liver, heart, and fat.
354 Components of mitochondrial respiratory chain complexes were the only complex subunits that had
355 significantly higher *D* than the proteome median (Fig. 6E), which is likely due to the dramatic differences
356 in mitochondrial lifetime across tissues (Fig. 5). Apart from these outliers, other multiprotein complex
357 subunits had average or significantly lower than average values of *D*. We noted that the small and large
358 subunits of the ribosome had extremely low *D* values (Fig. 6E), and that the stability of the small and large
359 subunits tracked very closely with each other (Fig. 6F). The ribosome also has a very consistent half-life
360 across fibroblasts derived from a range of mammalian species[17], indicating that ribosome turnover is very
361 tightly controlled. However, Rpl10 and Rps25 had much more variable k_{deg} values than other ribosomal
362 proteins (Fig. 6E,F). Interestingly, Rpl10 association is a key late regulatory step in large subunit
363 biogenesis[60], and Rps25 is incorporated only in a subset of ribosomes that are endowed with unique
364 translational specificity[61]. Rpl10 turns over faster than other large subunit components in the liver and
365 intestine, while Rps25 turns over faster than most small subunit components in the heart (Fig. 6F). These
366 data suggest nodes of ribosome biogenesis control that vary across tissues.
367
368 **Analysis of the effect of pathological aging on protein and cell homeostasis**
369 As aging progresses, the robustness of the proteostasis network declines[1] and proliferative cell
370 types undergo senescence and/or death. To model how aging affects tissue homeostasis, we applied
371 TRAIL to a mouse model of Hutchinson-Gilford progeria syndrome (HGPS), an accelerated aging disorder
372 that recapitulates many phenotypes of the aging process at a rapid rate[24,62]. HGPS is caused by an
373 autosomal dominant mutation to the *LMNA* gene, which encodes the broadly expressed nuclear structural
374 protein Lamin A[63]. Prominent symptoms of HGPS include loss of subcutaneous fat and hair, bone
375 weakening, and rapidly advancing cardiovascular disease[64].
376
377 We reprised our 6-timepoint, 32-day SILAM labeling timecourse in 9-week-old mice harboring the
378 HGPS-causative $LMNA^{G609G/+}$ mutation[62]. $LMNA^{G609G/+}$ mice exhibit progressive weight loss, bone
379 abnormalities, atherosclerosis, and cardiac abnormalities before succumbing to the disease between 9
380 and 12 months of age[62]. We focused our analyses on young adult (9-week-old) mice to evaluate early
381 changes to tissue homeostasis, and quantified cell lifetimes (Fig. 7A,B) and protein lifetimes (Fig. 7C,D) in
382 the intestine, liver, fat, and heart. Cell doubling times were similar in progeroid and healthy tissues (Fig.

383 7A, B), with one notable exception: the adipose tissue, where progeroid cells had a doubling time of ~55
384 days while age-matched wild type cells had a doubling time of ~78 days (Fig. 7B). In healthy fat, adipocyte
385 progenitors proliferate infrequently to produce long-lived fat-storing adipocytes. Our data indicate that the
386 proportion of proliferative cells is increased in progeroid fat, which could reflect more frequent proliferation
387 of progenitor cells and/or death of terminally differentiated cells. Notably, over-expression of the HGPS-
388 causative "progerin" mutant protein blocks the terminal differentiation of adipocyte precursors[65], and HGPS
389 patients suffer from severe lipodystrophy[64]. We speculate that *LMNA*$^{G609G/+}$ mice are in the early stages of
390 lipodystrophy at 9 weeks of age, as young adult animals are indistinguishable in weight compared to
391 littermates[62] although fat depots were modestly decreased in size (not shown).
392
393 We defined protein k_t values and corresponding predicted half-life ($t_{1/2}$) values for 2744 proteins in
394 the large intestine, 2098 proteins in the liver, 1429 proteins in the white adipose tissue, and 1608 proteins
395 in the heart (Supplementary Fig. 10). We then determined cell cycle-corrected k_{deg} values and predicted
396 $t_{1/2corr}$ values for the 849 proteins that we detected in the progeroid liver, heart, and fat (Fig. 7C,D). As we
397 previously observed in wild type animals, proteins generally turn over more rapidly in the progeroid liver
398 (median $t_{1/2corr}$ 3.3 days) than in the progeroid heart (median $t_{1/2corr}$ 6.8 days) or fat (median $t_{1/2corr}$ 8.2 days).
399 Interestingly, these data indicate global changes in protein stability in diseased *versus* healthy tissue:
400 proteins turn over significantly more slowly in diseased liver, fat, and heart than in age-matched healthy
401 tissue (Fig. 7D, WT data for the same 849 proteins reproduced in gray). This effect is most pronounced in
402 the progeroid heart and fat, where the median half-life is extended by over a day compared to age-matched
403 wild-type animals. Decreased proteasome activity has been reported in fibroblasts derived from HGPS
404 patients[66,67], leading us to speculate that decreased flux through the proteasome could underlie the
405 extension of protein lifetimes that we observe.
406
407 We took advantage of our hyperplexed experimental design to explore a third dimension of tissue
408 homeostasis in progeria: proteome composition. This was accomplished by hyperplexing entire SILAM
409 timecourse sample sets from each genotype, including unlabeled "day 0" samples, in a single 16-plex TMT
410 experiment. By comparing the reporter tag ion intensities between unlabeled samples, relative steady-
411 state protein abundances can be defined in healthy *versus* progeroid tissue. We have previously applied
412 this approach to TMT-SILAC timecourses[25] and use this approach here to profile relative protein
413 abundance in the intestine, liver, heart, and fat of healthy and progeroid animals (Fig. 7E, F).
414
415 Overall, we found that the progeroid liver, intestine, and heart had modest changes in proteome
416 composition, while the fat was much more dramatically affected (Fig. 7E, F). The small group of proteins
417 that change dramatically in the progeroid heart include myosin subunits (MYL1, MYH1, MYH2) and

associated regulators (cMLCK, MYLPF) (Fig. 7F, cluster 4; Supplementary Fig. 11D). Cardiac myosin light

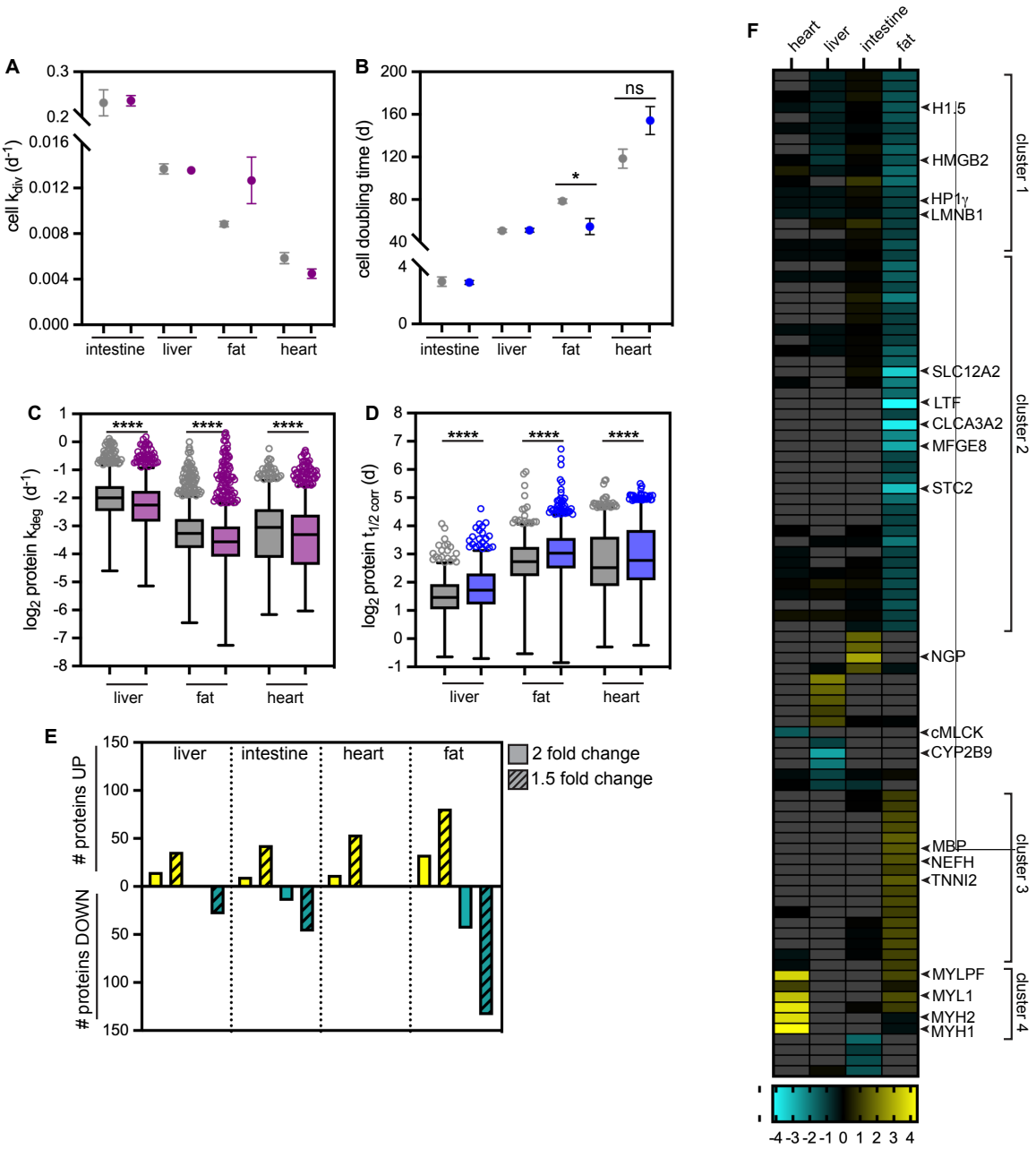

Figure 7. (A) Cell division rates (k_{div}) and (B) cell doubling times determined by SILAM-nucleotide SRM in labeled progeroid intestine, liver, fat, and heart. Wild type data from same tissues reproduced from Figure 3 in gray. Error bars, SEM. * indicates that progeroid fat cells have a significantly shorter doubling time than wild type fat cells ($p < 0.01$, t-test). See also Supplementary Table 7. (C) Cell-cycle-corrected degradation rates (k_{deg}) and (D) half-lives ($t_{1/2corr}$) for 849 proteins detected in both wild type and progeroid liver, fat, and heart. Box (Tukey) plot center line indicates median; boxes indicate 25th to 75th percentiles; whiskers indicate 1.5x interquartile range; points indicate outlier values. **** indicates that median proteome k_{deg} is lower in each progeroid tissue than in each wild type tissue ($p < 0.0001$, Kruskal-Wallis test). See also Supplementary Table 6 and 8 for complete datasets. (E) Number of proteins differentially expressed with more than a 1.5-fold difference (hashed bars) or a 2-fold difference (solid bars) in the progeroid liver, intestine, heart, and fat. (F) Heatmap of proteins exhibiting at least a 2-fold change in expression in liver, intestine, heart, or fat. Gray boxes indicate missing values (protein undetected). Proteins of interest in four major clusters indicated. See also Supplementary Table 9 for complete dataset.

420 chain kinase (cMLCK) is a key regulator of myosin-controlled contractility in the heart, and loss-of-function
421 mutations cause dilated cardiomyopathy in humans and mice[68,69]. While cMLCK loss of function has not
422 been previously linked to HGPS, progeroid mice and patients do exhibit cardiac conduction and contraction
423 defects[70]. Fat-specific disruptions included moderately decreased expression of chromatin factors such as
424 the linker histones H1.1 and H1.5, the chromatin-binding proteins HP1γ and HMGB2, and the nuclear
425 structural protein Lamin B1 (Fig. 7F, cluster 1; Supplementary Fig. 11A). Decreased HP1γ and Lamin B1
426 expression has also been reported in HGPS patient fibroblasts[71,72] and human iPSC models of HGPS[73,74].
427 We also noted that several proteins with major roles in regulating adiposity and/or body weight are potently
428 downregulated in progeroid fat, including lactadherin/MFGE8[75] and stanniocalcin-2 (STC2)[76] (Fig. 7F,
429 cluster 2; Supplementary Fig. 11B). On the other hand, neural and muscular proteins are more abundant
430 in progeroid fat, including the neurofilament proteins (NEFL, NEFM, and NEFH); myelin basic protein
431 (MBP), and troponin I (TNNI2) (Fig. 7F, cluster 3; Supplementary Fig. 11C). We speculate that these
432 dramatic changes may reflect the specific loss of adipocytes and proportional increase in the content of
433 peripheral nerves and muscular tissue in progeroid fat. Altogether, these protein abundance analyses
434 suggest that HGPS-linked disruption to nuclear organization also occurs in the fat (cluster 1), highlight a
435 novel progeria-linked change in cardiac tissue (cMLCK) and indicate major changes to adipose tissue
436 composition and function even at this early stage in 9-week-old progeroid animals (cluster 3).
437
438 **Discussion**
439 We have developed TRAIL, a multi-omic ^{15}N isotope labeling workflow that delivers protein
440 abundance, protein lifetime, and cellular lifetime data. To our knowledge, this is the first study to advance
441 a method for deriving cell turnover rates from ^{15}N labeling. While estimation of cellular turnover is commonly
442 achieved by pulse-labeling with nucleotide analogs such as ^{3}H-thymidine or BrdU or by D_2O incorporation
443 into the deoxyribose backbone of genomic DNA[20], each of these labels exerts some inherent toxicity and
444 interferes with the proliferation of some cell types[21–23]. This toxicity has enforced limits on both the length
445 of pulse-labeling that can be achieved and the tissues that can be accurately profiled[28]. ^{15}N, in contrast,
446 has no detectable toxicity even through multiple generations of labeling in mice[4,19], opening the possibility
447 of extending TRAIL to define turnover rates of slowly proliferating cell types. A second advantage of TRAIL
448 is its high precision; we track turnover of both purine and pyrimidine nucleosides using a label source at
449 100% isotope abundance, while other methods rely on pulse-labeling with lower doses of label[28].
450
451 By making parallel measurements of protein and cell turnover within tissues, we have been able to
452 evaluate protein homeostasis in tissue context. We have unambiguously determined that protein lifetimes
453 vary widely across tissues, and that both cell division and additional environmental factors shape protein
454 lifetime. Our data suggest that long-lived proteins experience a very different life cycle in post-mitotic

455 *versus* proliferative tissues. We found that dilution by cell division contributes extensively to the turnover
456 of about 15% of the proteome in the proliferative intestine, such that these proteins are renewed roughly
457 every 3 days as the epithelium renews. In contrast, these long-lived proteins turn over at slow rates in post-
458 mitotic tissues (the replication-dependent Histone H3.1 is an example). We speculate that only in this
459 context would long-lived proteins meaningfully "age" - meaning that they accumulate oxidative damage,
460 misfold, and lose their function. We have also uncovered evidence that the rate of organelle degradation,
461 perhaps by autophagy of peroxisomes, lipid droplets, and mitochondria, varies widely across tissues. Why
462 do some proteins turn over at such variable rates? It is possible that protein damage occurs more rapidly
463 in some tissues than in others, perhaps linked to the variable rate of production of reactive oxygen species
464 and other damaging agents during normal cellular metabolism. A second, non-exclusive possibility is that
465 the activity and/or selectivity of protein folding and/or degradation machineries varies across cell types and
466 tissues[45]. Intriguingly, *in vivo* reporters of the proteasome and of autophagy do suggest variable flux across
467 tissues[44,46].
468
469 We applied TRAIL to Hutchinson-Gilford progeria syndrome (HGPS) and uncovered disease-linked
470 disruptions to cell lifetime, proteome turnover, and proteome composition. We found that proteome
471 turnover rates are significantly decreased in progeroid tissues, and speculate that decreased proteasomal
472 activity could underlie this phenomenon. We took advantage of our hyperplexed experimental design to
473 evaluate the relative abundance of proteins in healthy *versus* progeroid tissues and uncovered a range of
474 tissue-specific differences, only some of which have been previously reported. For instance, Lamin B1 and
475 HP1γ moderately decrease in progeroid fat, as has been previously reported in patient fibroblasts[71,72] and
476 hiPSC models of HGPS[73,74]. However, this phenotype was only apparent in the fat tissue (Fig. 7). In the
477 heart, in contrast, we found alterations in proteins involved in cardiomyocyte contractility. One of these
478 proteins, cMLCK, has recently been linked to cardiomyopathy in humans[69]. Overall, these findings highlight
479 both global and tissue-specific features of HGPS.
480
481 There are some limitations of our approach to consider. Our pulse-labeling approach must assume
482 maintenance of homeostatic balance over the time frame of the experiment- an assumption that is more
483 likely to be valid over shorter timescales and in healthy tissues, but may not prove to be true over longer
484 timescales or in diseased tissues. In fact, comparison of cell turnover rates across healthy and progeroid
485 tissues detected a clear signature of homeostatic disruption in progeroid fat (Fig. 7). The accelerated cell
486 turnover observed could result from increased cell death and/or increased cell proliferation. While
487 progressive lipodystrophy is a well-described phenotype in HGPS[64], we anticipate that TRAIL could be
488 used to reveal the consequences of other diseases on tissue homeostasis.

489 Our study does not address the contribution of different cell types to our bulk measurements of
490 protein lifetime or protein abundance. We surmise that our data most accurately reflect the turnover and
491 abundance of proteins that are broadly expressed in most cell types of the tissues analyzed. Overall, we
492 were able to profile the 1500-3000 most abundant proteins per tissue, which tend to be broadly expressed
493 and not cell-type-specific. Nevertheless, tissue atlases generated by single cell sequencing can provide a
494 useful framework for thinking about the likely cell types of origin for the proteins profiled in this study[77].
495 Future studies may involve sorting individual abundant cell types from tissues of interest in order to
496 generate cell type-resolved maps of cell and proteome lifetime.
497
498 **Methods**
499
500 **Metabolic labeling of mice and tissue isolation**
501 We designed a 6-timepoint, 32-day SILAM labeling timecourse (0, 2, 4, 8, 16, and 32 days of labeling) with
502 a total of 3 animals of both sexes per labeled timepoint, and 2 animals for the day 0 (unlabeled) timepoint.
503 Timecourses were performed in both wild type and *LMNA*$^{G609G/+}$ C57Bl/6 mice[62] at approximately 9 weeks
504 of age. ^{14}N and ^{15}N mouse chow was obtained from Silantes. Animals were first habituated to the chow
505 formulation by feeding ^{14}N (normisotopic) food for 1 week and monitoring animal weight. Animals
506 maintained normal weight through the duration of the timecourse. Animals were then transitioned to ^{15}N
507 chow throughout the labeling period (roughly 3 grams / animal / day). Animals were then sacrificed by CO_2
508 inhalation followed by cervical dislocation, followed by tissue dissection and flash freezing by submersion
509 in liquid nitrogen. These animal experiments were performed in compliance with relevant ethical
510 regulations and with approval by the Institutional Animal Care and Use Committee at UCSF (IACUC
511 protocol number AN178187, PI: A.B.).
512
513 **Protein extraction and sample preparation for LC-MS/MS**
514 *Protein extraction:* Approximately 30 milligrams of frozen tissue was excised on dry ice with a clean
515 razorblade and placed in a fresh tube. 100 uL of protein extraction buffer (PEB: 5% SDS, 100 mM TEAB,
516 protease and phosphatase inhibitors, pH ~7) was added to the tube. The tissue was rapidly minced with
517 clean dissection scissors on ice for 30-60 seconds until no large pieces remained. PEB was added to bring
518 the final volume to 600 uL, then the sample was transferred to a Dounce homogenizer. The sample was
519 homogenized for ~40 strokes with the tight pestle, then was transferred to a clean microcentrifuge tube.
520 The sample was then probe sonicated at 4C (10% amplitude, 10 seconds, 2 cycles) before being
521 centrifuged (21,000 x g, 11 minutes, 4C). The supernatant was transferred to a clean tube, and aliquots
522 were separated for proteomics and protein quantification by microBSA assay (Pierce).

523 *Trypsinization:* Samples were diluted to 1 mg/mL in 5% SDS, 100 mM TEAB, and 25 µg of protein from
524 each sample was reduced with dithiothreitol to 2 mM, followed by incubation at 55°C for 60 minutes.
525 Iodoacetamide was added to 10 mM and incubated in the dark at room temperature for 30 minutes to
526 alkylate the proteins. Phosphoric acid was added to 1.2%, followed by six volumes of 90% methanol, 100
527 mM TEAB. The resulting solution was added to S-Trap micros (Protifi), and centrifuged at 4,000 x g for 1
528 minute. The S-Traps containing trapped protein were washed twice by centrifuging through 90% methanol,
529 100 mM TEAB. 1 µg of trypsin was brought up in 20 µL of 100 mM TEAB and added to the S-Trap, followed
530 by an additional 20 µL of TEAB to ensure the sample did not dry out. The cap to the S-Trap was loosely
531 screwed on but not tightened to ensure the solution was not pushed out of the S-Trap during digestion.
532 Samples were placed in a humidity chamber at 37°C overnight. The next morning, the S-Trap was
533 centrifuged at 4,000 x g for 1 minute to collect the digested peptides. Sequential additions of 0.1% TFA in
534 acetonitrile and 0.1% TFA in 50% acetonitrile were added to the S-trap, centrifuged, and pooled. Samples
535 were frozen and dried down in a Speed Vac (Labconco) prior to TMTpro labeling.

536 *TMT labeling*: Samples were reconstituted in TEAB to 1 mg/mL, then labeled with TMTpro 16plex reagents
537 (Thermo Fisher) following the manufacturers protocol. Briefly, TMTpro tags were removed from the -20°C
538 freezer and allowed to come to room temperature, after which acetonitrile was added. Individual TMT tags
539 were added to respective samples, and the reaction was allowed to occur at room temperature for 1 hour.
540 5% hydroxylamine was added to quench the reaction, after which the samples for each experiment were
541 combined into a single tube. Since we performed quantitation on the unlabeled peptides, 0 day samples
542 were added to four of the unused channels, increasing the signal for the unlabeled peptides. TMTpro
543 tagged samples were frozen, dried down in the Speed Vac, and then desalted using homemade C18 spin
544 columns to remove excess tag prior to high pH fractionation.

545 *High pH Fractionation:* Homemade C18 spin columns were activated with two 50 µL washes of acetonitrile
546 via centrifugation, followed by equilibration with two 50 µL washes of 0.1% TFA. Desalted, TMTpro tagged
547 peptides were brought up in 50 µL of 0.1% TFA and added to the spin column. After centrifugation, the
548 column was washed once with water, then once with 10 mM ammonium hydroxide. Fractions were eluted
549 off the column with centrifugation by stepwise addition of 10 mM ammonium hydroxide with the following
550 concentrations of acetonitrile: 2%, 3.5%, 5%, 6.5%, 8%, 9.5%, 11%, 12.5%, 14%, 15.5%, 17%, 18.5%,
551 20%, 21.5%, 27%, and 50%. The sixteen fractions were concatenated down to 8 by combining fractions 1
552 and 9, 2 and 10, 3 and 11, etc. Fractionated samples were frozen, dried down in the Speed Vac, and
553 brought up in 0.1% TFA prior to mass spectrometry analysis.

554 **LC-MS/MS Analysis**

555 *Data collection:* Peptides from each fraction were injected onto a homemade 30 cm C18 column with 1.8
556 um beads (Sepax), with an Easy nLC-1200 HPLC (Thermo Fisher), connected to a Fusion Lumos Tribrid
557 mass spectrometer (Thermo Fisher). Solvent A was 0.1% formic acid in water, while solvent B was 0.1%
558 formic acid in 80% acetonitrile. Ions were introduced to the mass spectrometer using a Nanospray Flex
559 source operating at 2 kV. The gradient began at 3% B and held for 2 minutes, increased to 10% B over 7
560 minutes, increased to 38% B over 94 minutes, then ramped up to 90% B in 5 minutes and was held for 3
561 minutes, before returning to starting conditions in 2 minutes and re-equilibrating for 7 minutes, for a total
562 run time of 120 minutes. The Fusion Lumos was operated in data-dependent mode, employing the
563 MultiNotch Synchronized Precursor Selection MS3 method to increase quantitative accuracy[78]. The cycle
564 time was set to 3 seconds. Monoisotopic Precursor Selection (MIPS) was set to Peptide. The full scan was
565 done over a range of 400-1500 m/z, with a resolution of 120,000 at m/z of 200, an AGC target of 4e5, and
566 a maximum injection time of 50 ms. Peptides with a charge state between 2-5 were picked for
567 fragmentation. Precursor ions were fragmented by collision-induced dissociation (CID) using a collision
568 energy of 35% and an isolation width of 1.0 m/z. MS2 scans were collected in the ion trap with an AGC
569 target of 1e4 and a maximum injection time of 35 ms. MS3 scans were performed by fragmenting the 10
570 most intense fragment ions between 400-2000 m/z, excluding ions that were 40 m/z less and 10 m/z
571 greater than the precursor peptide, using higher energy collisional dissociation (HCD). MS3 ions were
572 detected in the Orbitrap with a resolution of 50,000 at m/z 200 over a scan range of 100-300 m/z. The
573 isolation width was set to 2 Da, the collision energy was 60%, the AGC was set to 1e5, and the maximum
574 injection time was set to 100 ms. Dynamic exclusion was set to 45 seconds.

575 *Data analysis*: Raw data was searched using the SEQUEST search engine within the Proteome Discoverer
576 software platform, version 2.4 (Thermo Fisher), using the Uniprot mouse database (downloaded January
577 2020). Trypsin was selected as the enzyme allowing up to 2 missed cleavages, with an MS1 mass
578 tolerance of 10 ppm, and an MS2 mass tolerance of 0.6 Da. Carbamidomethyl on cysteine, and TMTpro
579 on lysine and peptide N-terminus were set as a fixed modifications, while oxidation of methionine was set
580 as a variable modification. Percolator was used as the FDR calculator, filtering out peptides which had a
581 q-value greater than 0.01. Reporter ions were quantified using the Reporter Ions Quantifier node, with an
582 integration tolerance of 20 ppm, and the integration method being set to “most confident centroid”. Protein
583 abundances were calculated by summing the signal to noise of the reporter ions from each identified
584 peptide, while excluding any peptides with an isolation interference of greater than 30%, or SPS matches
585 less than 65%.

586 *Kinetic model:* The kinetic model applied in this study has been previously described[25]. Briefly, we are
587 assuming that protein synthesis is a zero order process, occurs at a constant fractional rate, and that that
588 the total protein concentration of each cell does not change during the experimental time-course. The

589 dilution of the protein pool due to cell division can be modeled as a first order exponential process. Thus,
590 the fractional turnover of unlabeled proteins during the labeling time course can be regarded as a first order
591 kinetic process that can be modelled based on the following exponential equation:

592 $$\text{fraction unlabeled protein}(t) = e^{-k_t * t} \quad (1)$$

593 And:

594 $$k_t = k_{deg} + k_{div}$$

595 Where:

596 k_t is the clearance rate (observed rate of fractional labeling), k_{deg} is the rate of protein degradation and
597 k_{div} is the rate of cell division.

598 The determination of k_t values were conducted as previously described[25] using the decay of the TMT
599 reporter signals of unlabeled proteins. Protein-level TMT reporter abundances for unlabeled proteins for
600 each replicate experiment were first normalized by dividing by the intensity of the t0 reporter and then the
601 replicate experiments were aggregated in a single kinetic curve. In fitting the exponential decay curves of
602 the unlabeled protein signals, a constant fractional baseline at infinite time was incorporated in the fitting
603 equation. The equation used for fitting the curves was therefore: $intensity = baseline + (1 - baseline) *$
604 $e^{-k_t * time}$. The goodness of fit for least squares fits were assessed by determining the R^2, P-value and t-
605 statistic of the fits (see Supp Table 1). For subsequent analyses, only protein k_t measurements that were
606 obtained from all three replicate experiments, incorporated data from 4 or more peptide spectral matches
607 (PSMs), and had t-statistic values greater than three were considered.

608 **Nucleic acid extraction and sample preparation for LC-MS/MS**

609 *Genomic DNA extraction:* Approximately 30 milligrams of frozen tissue was excised on dry ice with a clean
610 razorblade and placed in a fresh tube. 100 uL of TRIzol reagent (Invitrogen) was added and the tissue was
611 rapidly minced with clean dissection scissors on ice for 30-60 seconds until no large pieces remained. An
612 additional 400 uL of TRIzol was added, and the sample was then transferred to a Dounce homogenizer.
613 The tissue was subjected to ~40 strokes with the tight pestle until smooth, then transferred back to the
614 original tube. The sample was incubated for at least 5 minutes before the addition of 100 uL chloroform
615 followed by mixing and a further 3 minutes of incubation. The sample was then centrifuged (12,000 x g, 15
616 minutes, 4C) and the upper RNA-containing aqueous layer was discarded. 150 uL of absolute ethanol was
617 added to the remaining sample, then inverted several times to mix. After 3 minutes of incubation at room
618 temperature, the sample was centrifuged (2,000 x g, 5 minutes, 4C). The protein-containing supernatant

619 was removed, then the DNA-containing pellet was resuspended in 500 uL of absolute ethanol and
620 incubated for 30 minutes. The sample was then centrifuged (2,000 x g, 5 minutes, 4C), and the supernatant
621 discarded. Sequential washes were then repeated with 95%, 85%, and 75% ethanol, after which the pellet
622 was air-dried for 5-10 minutes. The pellet was then resuspended in 200 uL nuclease-free water (Ambion)
623 at 56C, then incubated at 56C with shaking for 30 minutes to resuspend the pure DNA. The sample was
624 centrifuged (12,000 x g, 10 minutes, 4C), then the supernatant containing pure DNA was moved to a clean
625 tube. DNA concentration was determined with a NanoDrop spectrophotometer.
626
627 *Digestion of genomic DNA to short oligonucleotides:* 3-5 micrograms of pure genomic DNA was diluted to
628 a 50 uL volume in nuclease-free water, then combined with 50 uL of 2x Dinucleotide Buffer (DB: 5 mU/uL
629 benzonase, 40 mU/uL shrimp alkaline phosphatase, 20 mM Tris pH 7.9, 100 mM NaCl, 20 mM MgCl2).
630 Samples were incubated overnight at 37C. Spin-X UF Concentrators (Corning) were rinsed with 200 uL
631 buffer (20 mM Tris pH 7.9, 100 mM NaCl, 20 mM MgCl2), then samples were applied and centrifuged
632 through (12,000 x g, 5 min, RT). The eluate was collected for analysis.
633
634 *Digestion of genomic DNA to mononucleosides:* We extracted mononucleosides from genomic DNA
635 similarly to a previously described method[36] with some modifications. 1-3 micrograms of pure genomic
636 DNA was diluted to a 50 uL volume in nuclease-free water, then combined with 50 uL of 2x Mononucleoside
637 Buffer (MB: 5 mU/uL benzonase, 40 mU/uL shrimp alkaline phosphatase, 60 uU/uL phosphodiesterase I,
638 20 mM Tris pH 7.9, 100 mM NaCl, and 20 mM MgCl2). Samples were incubated overnight at 37C. Spin-X
639 UF Concentrators (Corning) were rinsed with 200 uL buffer (20 mM Tris pH 7.9, 100 mM NaCl, 20 mM
640 MgCl2), then samples were applied and centrifuged through (12,000 x g, 5 min, RT). The eluate was
641 collected for analysis.
642
643 **Mononucleoside and Dinucleoside LC-MS/MS**

644 Mononucleotide analyses were carried out by adapting a previously described method[79] using a Dionex
645 Ultimate 3000 UHPLC coupled to a Q Exactive Plus mass spectrometer (Thermo Scientific). After
646 purification, analytes were separated on a Hypersil Gold 2.1 x 150 mm column, protected by a 2.1 x 10
647 mm Hypersil Gold guard column (Thermo Scientific). The mobile phases were A: 0.1% formic acid in water,
648 and B: 0.1% formic acid in acetonitrile. The flow rate was set to 400 µL/min, and the column oven was set
649 to 36°C. 10 µL of each sample was injected, and the analytes were eluted using the following gradient: 0
650 min- 0% B, 6 min- 0% B, 8.5 min- 80% B, 9.5 min- 80% B, 10 min- 0% B, 13 min- 0% B. The Q Exactive
651 Plus was operated in positive mode with a heated electrospray ionization (HESI) source. The spray voltage
652 was set to 3.5 kV, the sheath gas flow rate was set to 40, and the auxiliary gas flow rate set to 7, while the
653 capillary temperature was set to 320°C. A parallel reaction monitoring (PRM) method was used to quantify

654 the unlabeled nucleotide, along with all of its N15 isotopes in a single scan. This was accomplished by
655 using wide (8 m/z) isolation widths when selecting the nucleotides for fragmentation. By employing this
656 method, we were able to quantify the level of labeling by looking at the intensity of each N15 labeled base
657 in the MS2 scan. Fragment ions were detected in the Orbitrap with a resolution of 70,000 at m/z 200. Using
658 a high resolution MS2 scan allowed us to resolve N15 and C13 isotopes. Peak areas from the fragment
659 ions were extracted with a 10 ppm mass tolerance using the LC Quan node of the XCalibur software
660 (Thermo Scientific).

661 Dinucleotide analyses were carried out using the same instrumentation, column, mobile phases, column
662 temperature, and flow rate employed by the mononucleotide experiments. The gradient was changed to
663 optimize dinucleotide separation as follows: 0 min- 5% B, 0.5 min- 5% B, 2.5 min- 90% B, 3.25 min- 90%
664 B, 3.5 min- 5% B, 5.5 min- 5% B. The Q Exactive Plus was operated using the same tune settings as the
665 mononucleotide experiment. However, instead of a PRM method, a full scan method from 500-650 m/z
666 was developed to quantify the dinucleotides dCdC, TT, dAdA, and dGdG, along with their corresponding
667 N15 isotopes. Precursor ions were detected in the Orbitrap with a resolution of 140,000 at m/z 200, using
668 the high resolution MS1 scan to try to separate N15 and C13 isotopes as much as possible. Peak areas
669 from the fragment ions were extracted with a 10 ppm mass tolerance using the LC Quan node of the
670 XCalibur software (Thermo Scientific).

671 *Measurement of kdiv*

672 To accurately measure rates of cell division (k_{div}) while factoring in the effects of incomplete labeling and
673 nucleotide recycling, we considered the time-dependent labeling patterns of mononucleotides and
674 dinucleotides derived from genomic DNA. Upon initiation of ^{15}N labeling, newly synthesized DNA strands
675 can incorporate nucleotides from a precursor pool with potentially complex mixture of partially labeled
676 species (Supplementary Fig. 5A). For example, a newly incorporated deoxyadenosine (dA) can be derived
677 from fully ^{15}N-labeled nucleotides derived from the dietary source, partially labeled species (containing one
678 to four ^{15}N atoms) derived by biosynthesis from incompletely labeled ^{15}N precursors, and completely
679 unlabeled nucleotides derived from recycling. As an example, a typical labeling pattern for dA from one of
680 our intestine samples is shown in Supplementary Fig. 5B showing the shift in the isotopologue distribution
681 over time. After correcting for the natural isotopic distribution, the peaks with heavier non-monoisotopic
682 masses (+1, +2, +3, etc.) can be assumed to have been derived from newly synthesized strands. However,
683 the monoisotopic peak (0) can potentially have been derived from both the original unlabeled strand, as
684 well as newly synthesized strands that had incoroporated recycled unlabeled nucleotides. Therefore, it
685 may not be possible to accurately determine the ratio of new to old strands (and hence k_{div}) from the
686 mononucleotide data alone. The labeling pattern of dinucleotides (dAdA) resolves this ambiguity. The
687 isotopologue distribution of labeled (non-monoisotopic) peaks in the dinucleotides spectra are dependent

688 on the composition of the nucleotide precursor pool. The red envelope depicted in the dAdA spectra is the
689 pattern that would be expected if the precursor pool was composed solely of the labeled (non-
690 monoisotopic) species observed in the corresponding mononucleotide spectra (i.e. new strands did not
691 contain any recycled unlabeled nucleotides and the monoisotopic peaks observed in the mononucleotide
692 spectra were derived solely from old strands). If a significant fraction of the monoisotopic peaks observed
693 in the mononucleotide spectra represents recycled nucleotides within new strands, then the isotopologue
694 distribution of labeled nucleotides would shift accordingly (Supplementary Fig. 5C). Through regression
695 analyses, we determined that within all tissues and timepoints analyzed in this study, the isotopologue
696 distributions of the dinucleotide data could be best modeled based on the assumption that newly
697 synthesized strands had very low levels of fully unlabeled nucleotides. Hence, the fractional population of
698 labeled non-monoisotopic peaks within dinucleotide and mononucleotide data were consistent with each
699 other (Supplementary Fig. 5D) and could be used to determine the fractional population of new strands.
700 For each tissue, fractional labeling of mononucleotide and dinucleotides for all 4 bases were combined
701 and the aggregated dataset was fit to a single exponential equation to determine first order rate constant
702 for division (k_{div}) (Supplementary Figure 5).
703
704 **Analysis of Proteomic Data**
705
706 *Quality filtering and analysis of k_t values:* Proteomic data was acquired in the form of 16-plex TMT
707 replicates containing 2 full 6-timepoint timecourses (one from wild type animals and one from progeroid
708 animals). For each genotype within each TMT replicate, proteins were filtered to retain only those detected
709 with at least 3 peptide spectral matches (PSMs) in all timepoints. Proteins that met these criteria were then
710 filtered per genotype within each TMT replicate based on goodness of fit using the t-statistic (cutoff t-
711 statistic value of at least 3). Filtered k_t values for each tissue were separated into deciles. Proteins in the
712 top decile (fastest k_t) and bottom decile (slowest k_t) were subjected to gene ontology analysis to identify
713 biological processes (GO:BP) and cellular components (GO:CC) that were over-represented, using the
714 Gprofiler tool[80]. Redundant GO terms were filtered using ReVIGO[81], then subjected to hierarchical
715 clustering and presented in heatmap format with cell values corresponding to the significance of
716 enrichment for each term.
717
718 *Determination and analysis of cell-cycle corrected k_{deg} values*: Cell-cycle-corrected protein k_{deg} values were
719 determined by subtracting the cell doubling time *(k_{div})* for each tissue from the apparent protein turnover
720 rate *(k_t)* determined in that tissue. In the intestine, a significant proportion of the proteome had *Kdeg* rates
721 very similar to k_{div}. Gene ontology analyses of this subset of ~400 proteins was performed to identify
722 biological processes (GO:BP) and cellular components (GO:CC) that were over-represented, using

723 Gprofiler[80]. Redundant GO terms were filtered using ReVIGO[81], and a bubble plot of significance of
724 enrichment vs. similarity (semantic space) was generated using Prism (GraphPad), where bubble sizes
725 correspond to the number of proteins mapped to a term. To analyze trends in turnover for intrinsically
726 disordered proteins (IDPs), a list of curated and experimentally validated IDPs from the DisProt database[29]
727 was cross-referenced to k_{deg} values.
728
729 *Cross-tissue dispersion of k_{deg} values:* Cross-tissue dispersion *(D)* was calculated on a protein-by-protein
730 basis for all proteins detected in the liver, heart, and fat tissues. *D = variance / mean*, where variance (V)
731 is the average of the squared differences of each k_{deg} value from the mean k_{deg} value. Because *D* is
732 normalized to the mean k_{deg} value, it is independent of the magnitude of k_{deg} (see Supplementary Figure
733 6). Analysis of *D* by organelle was performed using annotations from MitoCarta[82] for mitochondrial proteins,
734 from a recent proximity labeling study for lipid droplets[83], and manually curated annotations from UniProt
735 for all other organelles. Only UniProt annotations that listed a specific organelle as the first affiliation were
736 retained to limit multi-localizing proteins.

737 *Intra-complex dispersion of k_{deg} values for multiprotein complexes*: A mouse proteome multiprotein
738 complex subunit annotation set from ComplexPortal[84] was used to search for multiprotein complexes with
739 at least 5 subunits detected in the liver, heart, intestine, or fat. Intra-complex dispersion for these
740 complexes was determined by calculating the dispersion *(d = variance / mean)* of k_{deg} values for all subunits
741 detected in a tissue.
742
743 *Determination of relative protein abundance within tissues*: To evaluate relative protein abundance within
744 tissues, technical replicate unlabeled wild type (WT) samples from each multiplexed TMT run were first
745 channel normalized, then the geometric mean was calculated to determine mean normalized intensities
746 for each biological replicate. Protein abundance was then length-normalized by dividing each protein's
747 normalized intensity by the number of amino acids. Finally, samples were normalized for comparison
748 across biological replicates by normalizing each channel to the maximum value detected. The geometric
749 mean abundance was calculated by determining the geometric mean of the length- and channel-
750 normalized protein abundance. These relative abundance values were used to explore the relationship
751 between protein abundance and protein half-life (see Supplementary Fig. 2).
752
753 *Identification of differentially expressed proteins in wild type versus progeroid tissues:* To compare protein
754 abundance in unlabeled wild type (WT) versus progeroid (HGPS) tissues, technical replicate unlabeled
755 WT and HGPS samples from each multiplexed TMT run were first channel normalized, then the geometric
756 mean was calculated to determine mean normalized intensities for each biological replicate. Fold change
757 values for each biological replicate were determined by dividing the mean HGPS normalized intensity by

758 the mean WT normalized intensity. Proteins were then quality filtered based on sequence coverage and
759 replicate detection: a minimum of 3 peptide-spectral matches (PSMs) was required for each protein, and
760 detection in a minimum of 2 replicates was required. The geometric mean fold change was determined for
761 proteins passing these quality filters. P-values and q-values were then calculated based on replicate fold
762 change values. For identification of significantly differentially expressed proteins, proteins detected in all 3
763 replicates were filtered to include only those proteins with a minimum 2-fold change and a minimum q-
764 value of 0.05 in at least one tissue. Proteins detected in only 2 replicates were separately filtered to identify
765 proteins with a reproducible minimum 2-fold change in at least one tissue. This subset of proteins was
766 subjected to hierarchical clustering and plotted in heatmap format with cell values corresponding to the
767 magnitude of the fold change in protein expression.
768

769 **Data Availability**

770 LC-MS/MS data have been deposited in the ProteomeXchange Consortium via the PRIDE partner
771 repository, accessible at www.ebi.ac.uk/pride. The accession codes will be included in the final manuscript.
772

773 **Author Contributions**

774

775 A.B. and S.G. conceptualized the TRAIL approach. J.Hasper performed in vivo labeling experiments,
776 tissue isolations, and protein and DNA extractions. J. Hryhorenko and K. W. prepared and ran samples for
777 LC-MS/MS. A.B., J.Hasper, K.W., and S.G. analyzed data. A.B. and S.G. prepared the figures. A.B., J.
778 Hasper, and S.G. wrote the manuscript.
779

780 **Acknowledgements**

781

782 We would like to acknowledge the Progeria Research Foundation (A.B.), the Chan Zuckerberg Biohub
783 (A.B.), and the National Institutes of Health (R35 GM119502 and S10 OD025242, S.G.) for funding
784 support. We thank Biao Wang, Esther Paolo Mirasol, Balyn Zaro, Regan Volk, Carlos Lizama Valenzuela,
785 Yana Blokhina, Galina Schmunk, and Gabrielle Servito for assistance with tissue dissections.
786

787 **References**

788

789 1. Taylor, R. C. & Dillin, A. Aging as an Event of Proteostasis Collapse. *Csh Perspect Biol* 3, a004440 (2011).

790 2. Koyuncu, S. *et al.* Rewiring of the ubiquitinated proteome determines ageing in C. elegans. *Nature* 596, 285–290
791 (2021).

792 3. Price, J. C., Guan, S., Burlingame, A., Prusiner, S. B. & Ghaemmaghami, S. Analysis of proteome dynamics in
793 the mouse brain. *Proc National Acad Sci* 107, 14508–14513 (2010).

794 4. Savas, J. N., Toyama, B. H., Xu, T., III, J. R. Y. & Hetzer, M. W. Extremely Long-Lived Nuclear Pore Proteins
795 in the Rat Brain. *Science* 335, 942–942 (2012).

796 5. Toyama, B. H. *et al.* Identification of Long-Lived Proteins Reveals Exceptional Stability of Essential Cellular
797 Structures. *Cell* 154, 971–982 (2013).

798 6. Fornasiero, E. F. *et al.* Precisely measured protein lifetimes in the mouse brain reveal differences across tissues
799 and subcellular fractions. *Nature Communications* 9, 71–17 (2018).

800 7. Mathieson, T. *et al.* Systematic analysis of protein turnover in primary cells. *Nature Communications* 1–10
801 (2018).

802 8. Taylor, A. & Davies, K. J. A. Protein oxidation and loss of protease activity may lead to cataract formation in the
803 aged lens. *Free Radical Bio Med* 3, 371–377 (1987).

804 9. D'Angelo, M. A., Raices, M., Panowski, S. H. & Hetzer, M. W. Age-Dependent Deterioration of Nuclear Pore
805 Complexes Causes a Loss of Nuclear Integrity in Postmitotic Cells. *Cell* 136, 284–295 (2009).

806 10. Marrero, M. C. & Barrio-Hernandez, I. Toward Understanding the Biochemical Determinants of Protein
807 Degradation Rates. *Acs Omega* 6, 5091–5100 (2021).

808 11. Lee, R. van der *et al.* Intrinsically Disordered Segments Affect Protein Half-Life in the Cell and during
809 Evolution. *Cell Reports* 8, 1832–1844 (2014).

810 12. Fishbain, S. *et al.* Sequence composition of disordered regions fine-tunes protein half-life. *Nat Struct Mol Biol*
811 22, 214–221 (2015).

812 13. Wu, C. *et al.* Global and Site-Specific Effect of Phosphorylation on Protein Turnover. *Dev Cell* 56, 111-124.e6
813 (2021).

814 14. Zecha, J. *et al.* Linking post-translational modifications and protein turnover by site-resolved protein turnover
815 profiling. *Nat Commun* 13, 165 (2022).

816 15. Mallik, S. & Kundu, S. Topology and Oligomerization of Mono- and Oligomeric Proteins Regulate Their Half-
817 Lives in the Cell. *Structure* 26, 869-878.e3 (2018).

818 16. Dörrbaum, A. R., Kochen, L., Langer, J. D. & Schuman, E. M. Local and global influences on protein turnover
819 in neurons and glia. *eLife* 7, 489 (2018).

820 17. Swovick, K. *et al.* Cross-species Comparison of Proteome Turnover Kinetics*. *Journal Title Molecular and*
821 *Cellular Proteomics* 17, 580–591 (2020).

822 18. Matsuda, M. *et al.* Species-specific segmentation clock periods are due to differential biochemical reaction
823 speeds. *Science* 369, 1450–1455 (2020).

824 19. McClatchy, D. B., Dong, M.-Q., Wu, C. C., Venable, J. D. & Yates, J. R. 15N Metabolic Labeling of
825 Mammalian Tissue with Slow Protein Turnover. *J Proteome Res* 6, 2005–2010 (2007).

826 20. Macallan, D. C. *et al.* Measurement of cell proliferation by labeling of DNA with stable isotope-labeled
827 glucose: studies in vitro, in animals, and in humans. *P Natl Acad Sci Usa* 95, 708–13 (1998).

828 21. Reome, J. B. *et al.* The Effects of Prolonged Administration of 5-Bromodeoxyuridine on Cells of the Immune
829 System. *J Immunol* 165, 4226–4230 (2000).

830 22. Asher, E., Payne, C. M. & Bernstein, C. Evaluation of Cell Death in EB V-Transformed Lymphocytes Using
831 Agarose Gel Electrophoresis, Light Microscopy and Electron Microscopy: II. Induction of Non-Classic Apoptosis
832 ("Para-Apoptosis") by Tritiated Thymidine. *Leukemia Lymphoma* 19, 107–119 (2009).

833 23. Adams, W. H. & Adams, D. G. Effects of deuteration on hematopoiesis in the mouse. *J Pharmacol Exp Ther*
834 244, 633–9 (1988).

835 24. Gordon, L. B., Rothman, F. G., López-Otín, C. & Misteli, T. Progeria: A Paradigm for Translational Medicine.
836 *Cell* 156, 400–407 (2014).

837 25. Welle, K. A. *et al.* Time-resolved Analysis of Proteome Dynamics by Tandem Mass Tags and Stable Isotope
838 Labeling in Cell Culture (TMT-SILAC) Hyperplexing*. *Mol Cell Proteomics* 15, 3551–3563 (2016).

839 26. Guan, S., Price, J. C., Ghaemmaghami, S., Prusiner, S. B. & Burlingame, A. L. Compartment Modeling for
840 Mammalian Protein Turnover Studies by Stable Isotope Metabolic Labeling. *Anal Chem* 84, 4014–4021 (2012).

841 27. Guan, S., Price, J. C., Prusiner, S. B., Ghaemmaghami, S. & Burlingame, A. L. A Data Processing Pipeline for
842 Mammalian Proteome Dynamics Studies Using Stable Isotope Metabolic Labeling*. *Mol Cell Proteomics* 10,
843 M111.010728 (2011).

844 28. Sender, R. & Milo, R. The distribution of cellular turnover in the human body. *Nature Medicine* 1–15 (2021).

845 29. Quaglia, F. *et al.* DisProt in 2022: improved quality and accessibility of protein intrinsic disorder annotation.
846 *Nucleic Acids Res* 50, D480–D487 (2021).

847 30. Krishna, S. *et al.* Identification of long-lived proteins in the mitochondria reveals increased stability of the
848 electron transport chain. *Dev Cell* (2021) doi:10.1016/j.devcel.2021.10.008.

849 31. Bomba-Warczak, E., Edassery, S. L., Hark, T. J. & Savas, J. N. Long-lived mitochondrial cristae proteins in
850 mouse heart and brain. *J Cell Biol* 220, e202005193 (2021).

851 32. Drigo, R. A. e *et al.* Age Mosaicism across Multiple Scales in Adult Tissues. *Cell Metab* 30, 343-351.e3 (2019).

852 33. Neese, R. A. *et al.* Measurement in vivo of proliferation rates of slow turnover cells by 2H2O labeling of the
853 deoxyribose moiety of DNA. *Proceedings of the National Academy of Sciences* 99, 15345–15350 (2002).

854 34. Liao, Q., Chiu, N. H. L., Shen, C., Chen, Y. & Vouros, P. Investigation of Enzymatic Behavior of
855 Benzonase/Alkaline Phosphatase in the Digestion of Oligonucleotides and DNA by ESI-LC/MS. *Anal Chem* 79,
856 1907–1917 (2007).

857 35. Reichard, P. Interactions Between Deoxyribonucleotide And DNA Synthesis. *Annu Rev Biochem* 57, 349–374
858 (1988).

859 36. Quinlivan, E. P. & III, J. F. G. DNA digestion to deoxyribonucleoside: A simplified one-step procedure.
860 *Analytical Biochemistry* 373, 383–385 (2008).

861 37. Darwich, A. S., Aslam, U., Ashcroft, D. M. & Rostami-Hodjegan, A. Meta-Analysis of the Turnover of
862 Intestinal Epithelia in Preclinical Animal Species and Humans. *Drug Metab Dispos* 42, 2016–2022 (2014).

863 38. MacDONALD, R. A. Lifespan of Liver Cells: Autoradiographic Study Using Tritiated Thymidine in Normal,
864 Cirrhotic, and Partially Hepatectomized Rats. *Arch Intern Med* 107, 335–343 (1961).

865 39. Malliaras, K. *et al.* Cardiomyocyte proliferation and progenitor cell recruitment underlie therapeutic
866 regeneration after myocardial infarction in the adult mouse heart. *Embo Mol Med* 5, 191–209 (2013).

867 40. Rigamonti, A., Brennand, K., Lau, F. & Cowan, C. A. Rapid Cellular Turnover in Adipose Tissue. *Plos One* 6,
868 e17637 (2011).

869 41. Wu, R. S., Tsai, S. & Bonner, W. M. Patterns of histone variant synthesis can distinguish go from G1 cells. *Cell*
870 31, 367–374 (1982).

871 42. Ahmad, K. & Henikoff, S. The Histone Variant H3.3 Marks Active Chromatin by Replication-Independent
872 Nucleosome Assembly. *Mol Cell* 9, 1191–1200 (2002).

873 43. Cook, A. J. L., Gurard-Levin, Z. A., Vassias, I. & Almouzni, G. A Specific Function for the Histone Chaperone
874 NASP to Fine-Tune a Reservoir of Soluble H3-H4 in the Histone Supply Chain. *Mol Cell* 44, 918–927 (2011).

875 44. Mizushima, N., Yamamoto, A., Matsui, M., Yoshimori, T. & Ohsumi, Y. In vivo analysis of autophagy in
876 response to nutrient starvation using transgenic mice expressing a fluorescent autophagosome marker. *Molecular*
877 *Biology of the Cell* 15, 1101–1111 (2004).

878 45. Vonk, W. I. M. *et al.* Differentiation Drives Widespread Rewiring of the Neural Stem Cell Chaperone Network.
879 *Mol Cell* 78, 329-345.e9 (2020).

880 46. Jenkins, E. C. *et al.* Proteasome mapping reveals sexual dimorphism in tissue-specific sensitivity to protein
881 aggregations. *Embo Rep* 21, e48978 (2020).

882 47. Jr, W. A. D. *et al.* Pexophagy: The Selective Autophagy of Peroxisomes. *Autophagy* 1, 75–83 (2005).

883 48. Singh, R. *et al.* Autophagy regulates lipid metabolism. *Nature* 458, 1131–1135 (2009).

884 49. Youle, R. J. & Narendra, D. P. Mechanisms of mitophagy. *Nat Rev Mol Cell Bio* 12, 9–14 (2011).

885 50. Monastyrska, I. & Klionsky, D. J. Autophagy in organelle homeostasis: Peroxisome turnover. *Mol Aspects Med*
886 27, 483–494 (2006).

887 51. Zechner, R., Madeo, F. & Kratky, D. Cytosolic lipolysis and lipophagy: two sides of the same coin. *Nat Rev*
888 *Mol Cell Bio* 18, 671–684 (2017).

889 52. Lafontan, M. & Langin, D. Lipolysis and lipid mobilization in human adipose tissue. *Prog Lipid Res* 48, 275–
890 297 (2009).

891 53. Pascual, F. & Coleman, R. A. Fuel availability and fate in cardiac metabolism: A tale of two substrates.
892 *Biochimica Et Biophysica Acta Bba - Mol Cell Biology Lipids* 1861, 1425–1433 (2016).

893 54. Lau, E. *et al.* A large dataset of protein dynamics in the mammalian heart proteome. *Scientific Data* 3, 160015–
894 15 (2016).

895 55. McWilliams, T. G. *et al.* mito-QC illuminates mitophagy and mitochondrial architecture in vivo. *J Cell Biol*
896 214, 333–345 (2016).

897 56. Winter, D. & Becker, T. Surveying the mitochondrial proteome. *Nat Cell Biol* 23, 1216–1217 (2021).

898 57. Altshuler-Keylin, S. *et al.* Beige Adipocyte Maintenance Is Regulated by Autophagy-Induced Mitochondrial
899 Clearance. *Cell Metab* 24, 402–419 (2016).

900 58. McShane, E. *et al.* Kinetic Analysis of Protein Stability Reveals Age-Dependent Degradation. *Cell* 167, 803-
901 815.e21 (2016).

902 59. Matera, A. G. & Wang, Z. A day in the life of the spliceosome. *Nat Rev Mol Cell Bio* 15, 108–121 (2014).

903 60. Bussiere, C., Hashem, Y., Arora, S., Frank, J. & Johnson, A. W. Integrity of the P-site is probed during
904 maturation of the 60S ribosomal subunit. *J Cell Biol* 197, 747–759 (2012).

905 61. Shi, Z. *et al.* Heterogeneous Ribosomes Preferentially Translate Distinct Subpools of mRNAs Genome-wide.
906 *Mol Cell* 67, 71-83.e7 (2017).

907 62. Osorio, F. G. *et al.* Splicing-directed therapy in a new mouse model of human accelerated aging. *Science*
908 *translational medicine* 3, 106ra107-106ra107 (2011).

909 63. Eriksson, M. *et al.* Recurrent de novo point mutations in lamin A cause Hutchinson-Gilford progeria syndrome.
910 *Nature* 423, 293–298 (2003).

911 64. Merideth, M. A. *et al.* Phenotype and course of Hutchinson-Gilford progeria syndrome. *The New England*
912 *journal of medicine* 358, 592–604 (2008).

913 65. Scaffidi, P. & Misteli, T. Lamin A-dependent misregulation of adult stem cells associated with accelerated
914 ageing. *Nature Cell Biology* 10, 452–459 (2008).

915 66. Gabriel, D., Roedl, D., Gordon, L. B. & Djabali, K. Sulforaphane enhances progerin clearance in Hutchinson-
916 Gilford progeria fibroblasts. *Aging Cell* 14, 78–91 (2014).

917 67. Buchwalter, A. & Hetzer, M. W. Nucleolar expansion and elevated protein translation in premature aging.
918 *Nature Communications* 1–13 (2017).

919 68. Massengill, M. T. *et al.* Acute heart failure with cardiomyocyte atrophy induced in adult mice by ablation of
920 cardiac myosin light chain kinase. *Cardiovasc Res* 111, 34–43 (2016).

921 69. Tobita, T. *et al.* Identification of MYLK3 mutations in familial dilated cardiomyopathy. *Sci Rep-uk* 7, 17495
922 (2017).

923 70. Benedicto, I., Dorado, B. & Andrés, V. Molecular and Cellular Mechanisms Driving Cardiovascular Disease in
924 Hutchinson-Gilford Progeria Syndrome: Lessons Learned from Animal Models. *Cells* 10, 1157 (2021).

925 71. Scaffidi, P. & Misteli, T. Lamin A-Dependent Nuclear Defects in Human Aging. *Science* 312, 1059–1063
926 (2006).

927 72. Kubben, N., Brimacombe, K. R., Donegan, M., Li, Z. & Misteli, T. A high-content imaging-based screening
928 pipeline for the systematic identification of anti-progeroid compounds. *Methods* 96, 46–58 (2016).

929 73. Liu, G.-H. *et al.* Recapitulation of premature ageing with iPSCs from Hutchinson-Gilford progeria syndrome.
930 *Nature* 472, 221–225 (2011).

931 74. Zhang, J. *et al.* A Human iPSC Model of Hutchinson Gilford Progeria Reveals Vascular Smooth Muscle and
932 Mesenchymal Stem Cell Defects. *Cell Stem Cell* 8, 31–45 (2011).

933 75. Khalifeh-Soltani, A. *et al.* Mfge8 promotes obesity by mediating the uptake of dietary fats and serum fatty
934 acids. *Nat Med* 20, 175–183 (2014).

935 76. Jiao, Y. *et al.* Stanniocalcin2 acts as an anorectic factor through activation of STAT3 pathway. *Oncotarget* 8,
936 91067–91075 (2017).

937 77. Neff, N. F. *et al.* Single-cell transcriptomics of 20 mouse organs creates a Tabula Muris. *Nature* 1–25 (2018).

938 78. McAlister, G. C. *et al.* MultiNotch MS3 Enables Accurate, Sensitive, and Multiplexed Detection of Differential
939 Expression across Cancer Cell Line Proteomes. *Anal Chem* 86, 7150–7158 (2014).

940 79. Su, D. *et al.* Quantitative analysis of ribonucleoside modifications in tRNA by HPLC-coupled mass
941 spectrometry. *Nat Protoc* 9, 828–841 (2014).

942 80. Raudvere, U. *et al.* g:Profiler: a web server for functional enrichment analysis and conversions of gene lists
943 (2019 update). *Nucleic Acids Res* 47, W191–W198 (2019).

944 81. Supek, F., Bošnjak, M., Škunca, N. & Šmuc, T. REVIGO Summarizes and Visualizes Long Lists of Gene
945 Ontology Terms. *Plos One* 6, e21800 (2011).

946 82. Rath, S. *et al.* MitoCarta3.0: an updated mitochondrial proteome now with sub-organelle localization and
947 pathway annotations. *Nucleic Acids Res* 49, gkaa1011- (2020).

948 83. Bersuker, K. *et al.* A Proximity Labeling Strategy Provides Insights into the Composition and Dynamics of
949 Lipid Droplet Proteomes. *Dev Cell* 44, 97-112.e7 (2018).

950 84. Meldal, B. H. M. *et al.* Complex Portal 2018: extended content and enhanced visualization tools for
951 macromolecular complexes. *Nucleic Acids Res* 47, gky1001- (2018).

952